

JGR Atmospheres



RESEARCH ARTICLE

10.1029/2021JD036039

Key Points:

- Specular meteor radar (SMR) vertical velocities are assessed for the first time using a high-resolution forward model
- The validation analyses suggest that mean horizontal winds and gradients estimation techniques used in multistatic SMRs work effectively
- Tide-like periodicities observed in vertical winds using multistatic SMRs are not reproduced by horizontal wind component aliasing

Supporting Information:

Supporting Information may be found in the online version of this article.

Correspondence to:

H. Charuvil Asokan, hari@iap-kborn.de

Citation:

Charuvil Asokan, H., Chau, J. L., Larsen, M. F., Conte, J. F., Marino, R., Vierinen, J., et al. (2022). Validation of multistatic meteor radar analysis using modeled mesospheric dynamics: An assessment of the reliability of gradients and vertical velocities. *Journal of Geophysical Research: Atmospheres*, 127, e2021JD036039. https://doi.org/10.1029/2021JD036039

Received 13 OCT 2021 Accepted 22 FEB 2022

Author Contributions:

Conceptualization: Harikrishnan Charuvil Asokan, Jorge L. Chau Data curation: Harikrishnan Charuvil Asokan, Jorge L. Chau, J. Federico Conte, Sebastian Borchert Formal analysis: Harikrishnan Charuvil Asokan, Juha Vierinen

Funding acquisition: Jorge L. Chau **Investigation:** Harikrishnan Charuvil Asokan, Jorge L. Chau

© 2022. The Authors.

This is an open access article under the terms of the Creative Commons Attribution-NonCommercial-NoDerivs License, which permits use and distribution in any medium, provided the original work is properly cited, the use is non-commercial and no modifications or adaptations are made.

Validation of Multistatic Meteor Radar Analysis Using Modeled Mesospheric Dynamics: An Assessment of the Reliability of Gradients and Vertical Velocities

Harikrishnan Charuvil Asokan^{1,2}, Jorge L. Chau¹, Miguel F. Larsen³, J. Federico Conte¹, Raffaele Marino², Juha Vierinen⁴, Gerd Baumgarten¹, and Sebastian Borchert⁵

¹Leibniz-Institute of Atmospheric Physics at the Rostock University, Kühlungsborn, Germany, ²Laboratoire de Mécanique des Fluides et d'Acoustique, UMR5509, Université de Lyon, CNRS, ÉCole Centrale de Lyon, INSA de Lyon, Université Claude Bernard Lyon 1, Écully, France, ³Department of Physics and Astronomy, Clemson University, Clemson, SC, USA, ⁴Department of Physics and Technology, University of Tromsø, The Arctic University of Norway, Tromsø, Norway, ⁵Deutscher Wetterdienst, Offenbach am Main, Germany

Abstract A virtual meteor radar system based on the upper-atmosphere extension of the high-resolution ICOsahedral Non-hydrostatic general circulation model is constructed to validate multistatic specular meteor radar (SMR) analyses. The virtual radar system examines the validity of mean winds and gradients estimation techniques used in multistatic SMRs. The study is motivated by unexpected mean values and tide-like features recently observed in the vertical velocities estimated from multistatic SMRs at different latitudes in the mesosphere and lower thermosphere. The proposed analysis confirms multistatic SMR systems' excellent capability to measure the horizontal mean wind components and gradient terms. It is also found that multistatic SMRs can estimate mean vertical winds if they have an amplitude greater than ± 2 m/s. Due to the smoothing inherent to the model results, these results should be treated as lower bounds to the error incurred using real data. Hourly variability in vertical velocity estimates up to $\pm 1-2$ m/s in the observed vertical winds are due to contamination by small-scale horizontal structures in the horizontal winds.

Plain Language Summary Specular meteor radars (SMRs) are a prominent ground-based instrument to study the mesosphere and the lower thermosphere dynamics. Recently developed multistatic SMRs allow maximizing the number of measurements from different viewing angles, enabling the estimation of horizontal wind fields and their second-order statistics (power spectrum, momentum fluxes). We have implemented the operational versions of these techniques in Germany, Peru, and Argentina called Spread-spectrum Interferometric Multistatic meteor radar Observing Network (SIMONe) systems. We present a validation study of multistatic SMR analyses using virtual radar systems using as an input the prognostic fields obtained from the UA-ICON general circulation model with a horizontal grid spacing of 5 km. The study focuses on the estimates of gradients and vertical velocities based on these multistatic systems.

1. Introduction

The mesosphere and lower thermosphere (MLT) is a dynamically active region representing the boundary between the neutral atmosphere and space. This region is permeated by atmospheric tides, planetary waves, and gravity waves, which play key roles in coupling the lower and upper strata of the atmosphere (Alexander et al., 2010; Fritts & Alexander, 2003; Smith, 2012; Vincent, 2015). Continuous observations of the MLT have always been a difficult task. Historically, a few ground-based instruments like lidars, optical imagers, and different radars have contributed to further the understanding of MLT dynamics (e.g., Chen et al., 2016; Gerding et al., 2021; Hecht et al., 2010; Hibbins et al., 2007; Hoffmann et al., 2010; Huang et al., 2021; Larsen, 2004; Liu et al., 2020; Lübken et al., 2011; Murphy et al., 2009; Nakamura et al., 2001).

One main observable in the MLT is the wind velocity field. This is critical in order to understand the dynamics of small to large-scale atmospheric motions. Our study focuses on assessing the accuracy of winds estimated using multistatic Specular Meteor Radar (SMR) (multistatic SMR). Monostatic SMRs are widely used to study the dynamics of the atmosphere between 75 and 105 km above sea level (e.g., Forbes et al., 1999; Hocking & Hock-



Methodology: Harikrishnan Charuvil Asokan, Jorge L. Chau Project Administration: Jorge L. Chau Resources: Harikrishnan Charuvil Asokan, Miguel F. Larsen, J. Federico Conte, Raffaele Marino, Gerd Baumgarten, Sebastian Borchert Software: Harikrishnan Charuvil Asokan Supervision: Jorge L. Chau, Raffaele Marino

Validation: Harikrishnan Charuvil Asokan, Jorge L. Chau, Miguel F. Larsen, J. Federico Conte

Visualization: Harikrishnan Charuvil Asokan

Writing – original draft: Harikrishnan Charuvil Asokan

Writing – review & editing: Harikrishnan Charuvil Asokan, Jorge L. Chau, Miguel F. Larsen, J. Federico Conte, Raffaele Marino, Juha Vierinen, Gerd Baumgarten, Sebastian Borchert ing, 2002; Hocking, Fuller et al., 2001; Kishore Kumar & Hocking, 2010; Lima et al., 2004; Younger et al., 2015). By increasing the number of meteor detections and improving the viewing angle diversity, multistatic SMRs enhance the quality of mean horizontal wind and gradients estimation and second-order wind dynamics (e.g., momentum fluxes; Charuvil Asokan et al., 2021; Chau et al., 2017; Chau, Urco, et al., 2021; Conte et al., 2021; Spargo et al., 2019; Stober & Chau, 2015; Stober et al., 2021, 2018; Volz et al., 2021).

The background zonal and meridional winds obtained from SMRs have been studied for decades. For example, they have been extensively used to study atmospheric tides in the MLT, sudden stratospheric warmings and their impacts, the quasi 2-day wave and its effects, planetary wave activity, gravity waves and their effects in the MLT, etc (e.g., Abdu et al., 2006; Conte et al., 2017; De Wit et al., 2014; Eswaraiah et al., 2020; Fritts et al., 2002; He & Chau, 2019; Lilienthal & Jacobi, 2015; Lima et al., 2004; Mitchell & Beldon, 2009; Pancheva, 2004; Placke et al., 2011; Vincent et al., 2010; Xiong et al., 2004). The reliability of the estimation of mean horizontal winds from SMRs is not disputed. However, whether reliable estimates of vertical velocity can be performed with this type of radars has been debatable so far.

In most of the meteor radar analyses, the vertical winds (w) are assumed to be zero (w = 0), and this is rationalized based on the idea that the mean vertical velocity within a large observation volume (circa 400 km diameter, in the case of SMRs) is expected to be close to zero on average, assuming the statistical distribution of the vertical wind velocities is close to Gaussian (Cervera & Reid, 1995; Holdsworth et al., 2004; Marsh et al., 2000; McCormack et al., 2017; Nakamura et al., 1991). Only a few studies discuss the vertical velocity estimates from SMR data (Chang et al., 1999; Egito et al., 2016; Suresh Babu et al., 2012). Suresh Babu et al. (2012) examined the possibility of using only the meteor echoes centered at the meteor ablation peak to estimate all three wind components. Egito et al. (2016) followed this approach to measure vertical winds from an all-sky meteor radar over the Brazilian region. In their work, they found vertical velocities of a few m/s at MLT altitudes. Chau et al. (2017) disputed this approach by stating that those high magnitudes are partially the result of horizontal divergence contamination, which Egito et al. (2016) assumed to be non-existent in their analysis.

Chau et al. (2017) used a gradient approach to determine horizontal wind components and gradient terms directly from SMR and discarded the vertical velocity obtained using the homogeneous approach since their values are shown to be a consequence of horizontal divergence contamination. However, some of the recent analyses using multistatic SMRs motivate us to look more carefully into the problem of vertical velocity determination from SMRs. The main questions that will be addressed here are: Can we estimate vertical velocities and gradients using SMRs? If yes, how accurate are these results?

We present a validation study of multistatic SMR analyses using virtual meteor radar systems applied to a model atmosphere as simulated by the upper-atmosphere extension of the high-resolution ICOsahedral Non-hydrostatic (UA-ICON) general circulation model. The high-resolution configuration of the UA-ICON model allows to construct the virtual meteor radar due to the close and sparse sampling from multistatic SMRs. This validation study is similar to an observing system simulation experiment, a modeling experiment used to evaluate a new observing system when actual observational data are not present (Zeng et al., 2020). However, we will address our study as a validation study in the manuscript.

The manuscript is organized as follows. A section exploring previous efforts to estimate vertical velocities using SMRs and other ground-based instruments is proposed. Then, in Section 3, we describe the data sets used in our study. In Section 4, we introduce our methodologies to describe the virtual radar system setup. The main results and findings are presented in Section 5, and they are discussed in Section 6. Finally, the conclusions are presented in Section 7.

2. Previous Vertical Velocity Estimations From SMRs

In November 2018, we carried out a 7-day multistatic SMR campaign with 14 meteor radar links (Spread-spectrum Interferometric Multistatic meteor radar Observing Network [SIMONe] 2018, 54°N) (Charuvil Asokan et al., 2021; Vargas et al., 2021). Charuvil Asokan et al. (2021) focused on the frequency spectral studies of horizontal wind components using the Wind-field Correlation Function Inversion (WCFI) method described in Vierinen et al. (2019). In this study, we are intrigued by the hourly mean vertical wind values estimated using the gradient approach. These estimates had a standard deviation close to ± 3.2 m/s. Besides, they show a diurnal

CHARUVIL ASOKAN ET AL. 2 of 21



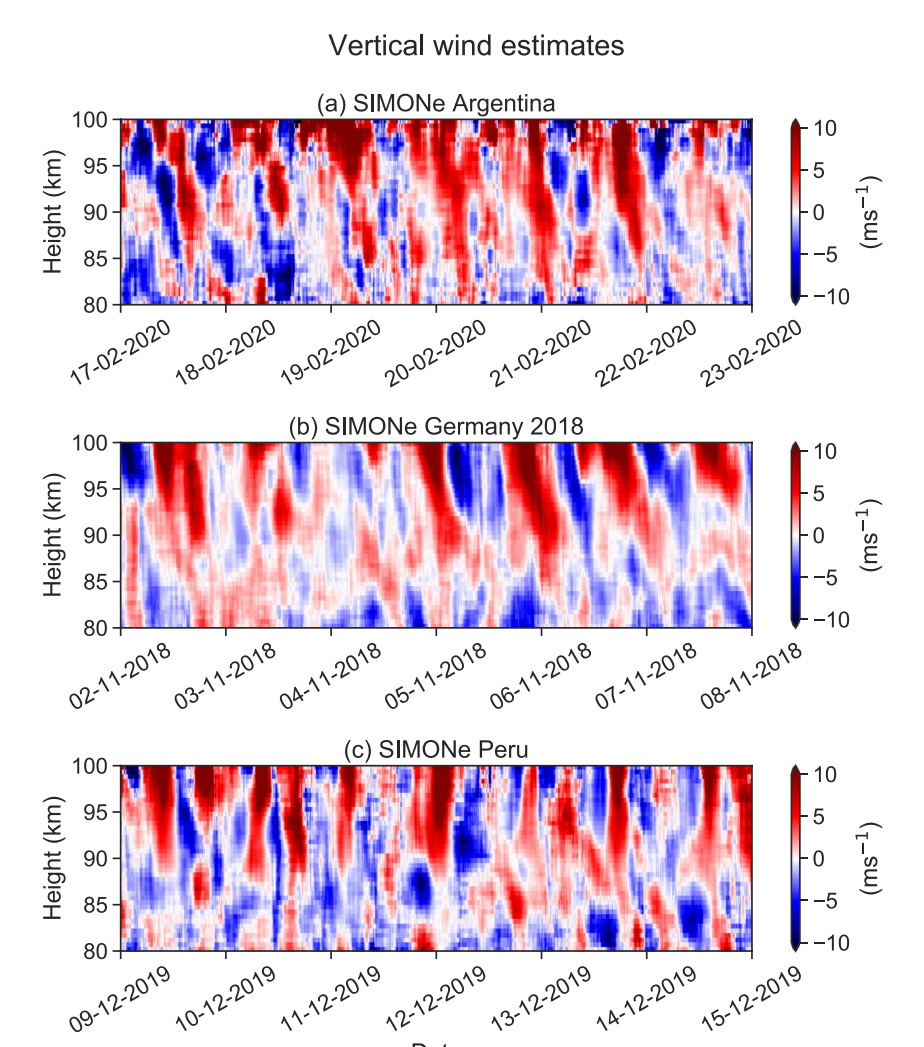


Figure 1. (a–c) show the estimated vertical velocities using SIMONe Argentina, SIMONe 2018 (Germany) and, SIMONe Peru for seven days. These winds were estimated using specular meteor events observed within 4 hr and 4 km time-altitude bins.

Date

behavior at high altitudes (90–100 km). Our motivation for this study originated from the consideration of the frequency spectra of vertical winds using the WCFI method. The vertical wind spectrum also showed a peak around the 24-hr period. Note that the WCFI spectrum does not use any functional form for the horizontal or vertical winds (Charuvil Asokan et al., 2021; Vierinen et al., 2019).

Since two independent analyses (i.e., the gradient approach and the WCFI method) showed a diurnal pattern in the vertical velocity, we looked into other multistatic systems such as SIMONe Argentina (50°S) and SIMONe Peru (12°S). We found unexpected high vertical velocity estimates using the gradient approach (refer Section 4.1) in both these systems (Chau, Urco et al., 2021; Conte et al., 2021). The vertical velocity estimates from SIMONe 2018, SIMONe Peru, and SIMONe Argentina are shown in Figure 1. For this figure, we used the exact dates of the analyses presented in Charuvil Asokan et al. (2021); Chau, Urco, et al. (2021); Conte et al. (2021). Notice that the vertical estimates from SIMONe Argentina and SIMONe 2018 show a diurnal pattern, while those from SIMONe Peru show a dominant semi-diurnal (12 hr) oscillation.

To check whether these tidal features are artifacts of the observational geometry, we selected another set of 7 days from Multistatic- Multi-frequency Agile Radar for Investigations of the Atmosphere (MMARIA)/ SIMONe Germany and SIMONe Peru. Figure 2 shows the 7-day composite daily mean plots of two data sets from Germany and Peru at different heights. Figure 2a shows data from SIMONe 2018 during the campaign

CHARUVIL ASOKAN ET AL. 3 of 21



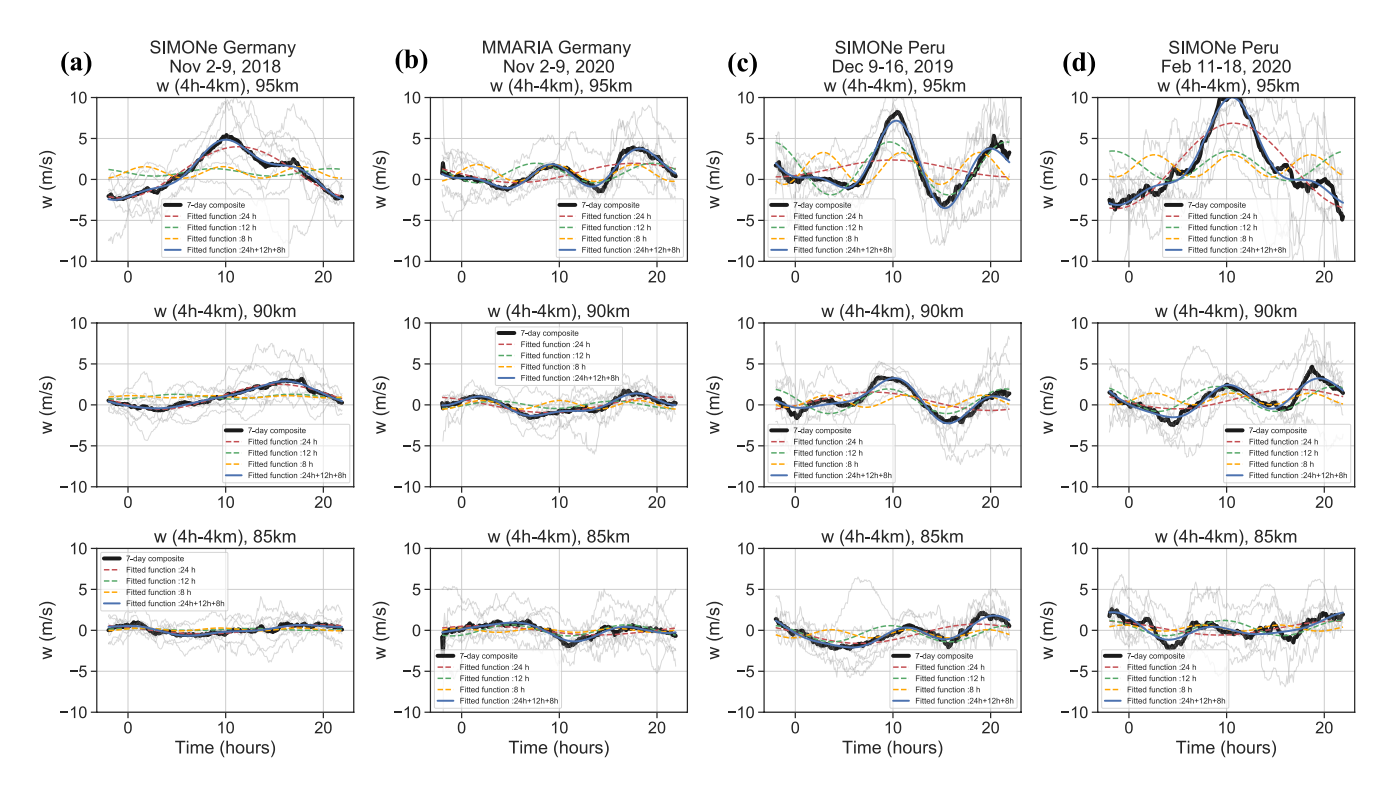


Figure 2. Seven-day composite daily mean vertical velocities for (a) SIMONe 2018 during the campaign (November 2–9, 2018), (b) MMARIA/SIMONe Germany from November 2–9, 2020, (c) SIMONe Peru from December 9–16, 2019 and, (d) SIMONe Peru from February 11–18, 2020. Each row in the figure displays the graphs corresponding to altitudes of (from top to bottom) 95, 90, and 85 km. The solid black lines on each graph show the composite average of 7 days, and the thin gray lines on each graph show the values for each of the 7 days. The colored lines show the fitted curves corresponding to the following periodic sine waves: red – 24 hr, green – 12 hr, orange – 8 hr, and blue – a sum of the 24, 12, and 8-hr waves.

(November 2–9, 2018), 2b of MMARIA/SIMONe Germany from November 2–9, 2020, 2c shows SIMONe Peru from December 9–16, 2019, and Figure 2d from February 11–18, 2020. The solid black lines on each graph show the composite average of 7 days, and thin gray lines on each graph show the daily values. In each plot, we fit the average with different periodic sine functions. The red dotted line corresponds to the 24-hr function, green to the 12-hr, and orange to the 8-hr. The blue line is the fit for a sum of periodic sine waves with periods of 8 hr, 12 hr, and 24 hr. These fitted lines show which period is dominant in the vertical velocity estimates. It is clear from the figures that the tidal features become more substantial with increasing altitude and that the prevailing periodicity is not always diurnal.

In previous observations, vertical velocities in the MLT were seldom reported. Since synoptic-scale vertical winds in the MLT are expected to be in the range of a few cm/s, it requires highly sophisticated and accurate measurements for reliable estimates. A recent climatological study on polar mesospheric summer echo (PMSE) mean vertical velocities discusses the difficulty of measuring mesospheric vertical winds (Gudadze et al., 2019).

Most of the synoptic-scale vertical wind studies based on observational methods derive amplitudes in the order of a few cm/s. However, these studies do not directly measure mean vertical velocities in the MLT because of their small values. Many of these studies rely on theoretical assumptions to estimate the winds. For example, Fauliot et al. (1997) used the Wind Imaging Interferometer on the Upper Atmosphere Research Satellite to derive vertical winds using the continuity equation. Dowdy et al. (2001); Laskar et al. (2017), and Vincent et al. (2019) inferred vertical velocities by measuring the horizontal wind divergence in the MLT using ground-based radars such as Medium Frequency (Partial Reflection) radars and SMRs. Such studies mostly agree with model calculations by Garcia (1989), which show small vertical winds in the MLT.

Studies using European Incoherent Scatter (EISCAT) very high requency radars have previously observed vertical velocities in the order of a few m/s (Fritts et al., 1990; Hoppe & Fritts, 1995a, 1995b; Lee et al., 2018; Mitchell & Howells, 1998; Vierinen et al., 2013). Incoherent scatter radars have been used to measure vertical velocities in

CHARUVIL ASOKAN ET AL. 4 of 21



the mesosphere (Hysell et al., 2014; Zhou, 2000). However, these studies are not comparable to multistatic SMRs, since they use smaller observing volumes. Recent PMSE observations showed 50 m/s extreme vertical drafts in the MLT region (Chau, Marino, et al., 2021). These sudden powerful drafts are large-scale intermittent events which have been observed also in direct numerical simulations of stratified turbulent flows in a parameter space compatible with the MLT (Feraco et al., 2018, 2021). They were found to emerge from the interplay of gravity waves and turbulent motions (Marino, Rosenberg, et al., 2015), enhancing dissipation and mixing (Marino et al., 2021), possibly acting as a local energy injection mechanism triggering direct and/or inverse cascades in stratified geophysical flows (Marino et al., 2013, 2014; Marino, Pouquet, et al., 2015; Marino, Rosenberg, et al., 2015; Pouquet et al., 2017).

Vertical velocities with magnitudes between 5 and 15 m/s lasting a few hours were observed using other instruments in the MLT (Gardner & Liu, 2007; Lehmacher et al., 2011) and thermosphere regions (Larsen & Meriwether, 2012).

Therefore, the magnitudes and duration are not that unusual. What is remarkable is that we observe such features in our multistatic SMRs after averaging over a horizontal area with an approximate 200 km radius. The motivation of our study mainly comes from the unexpected mean amplitudes and tidal features observed in the vertical velocities obtained from multistatic SMRs located at different latitudinal sectors of the world.

3. Data Sets

3.1. UA-ICON

The ICOsahedral Non-hydrostatic (ICON) general circulation model is a joint development of the Max Planck Institute for Meteorology in Hamburg, Germany, and the German Weather Service. ICON is developed based on a non-hydrostatic dynamical core with a triangular horizontal grid (Crueger et al., 2018; Dipankar et al., 2015; Giorgetta et al., 2018; Heinze et al., 2017; Zängl et al., 2015). Our study uses the UA-ICON model introduced by Borchert et al. (2019). The model output used in this study result from a simulation with horizontal grid nesting. Starting from a global domain with 20 km horizontal mesh size, there are two nested domains covering the region of interest. The mesh size of the first nest is 10 km, and the one of the second innermost nest is 5 km. The simulation uses 250 vertical grid layers that extend from the surface to 150 km. In order to damp gravity wave reflection from the rigid model top, a sponge layer acts above 110 km.

The reason for using simulations of the UA-ICON model is its relatively high spatial and temporal resolution. This allows a correspondingly frequent output of the simulated atmospheric state at MLT altitudes every 5 min on a grid with a horizontal spacing of 0.06° in latitude and longitude and a vertical level spacing of 600 m. This configuration of UA-ICON enables us to conduct our virtual multistatic meteor radar (VMMR) network efficiently. The methodology of the virtual system is described in Section 4.2.

3.2. SIMONe Systems

The inspiration for the SIMONe systems conceived by Chau and Clahsen (2019) originated from the following factors: The MMARIA concept (Stober & Chau, 2015), radar signal processing techniques for coded continuous wave meteor radar transmissions (Vierinen et al., 2016), multiple transmitters and multiple receivers (MIMO) for radar interferometry (Urco et al., 2018), and compressed sensing (Urco et al., 2019). A special campaign was conducted in northern Germany to test this concept for 7 days in November 2018. Results from this campaign were later used in Charuvil Asokan et al. (2021); Vargas et al. (2021); Vierinen et al. (2019). Henceforth, we call this data set SIMONe 2018. The campaign gave us a substantial amount of specular meteor observations that is 10 times larger than those of a typical monostatic SMR. SIMONe 2018 is comprised of 14 meteor radar links located in the northern part of Germany. Six of them were existing pulsed systems, and the remaining eight links were implemented with coded continuous wave transmissions with MIMO technology (refer to Charuvil Asokan et al. (2021) for more details about SIMONe 2018).

Operational versions of SIMONe systems were later installed in Peru and Argentina. These systems consist of one transmitter and five receiving stations and have been operating since September 2019 (Chau, Urco, et al., 2021; Conte et al., 2021).

CHARUVIL ASOKAN ET AL. 5 of 21

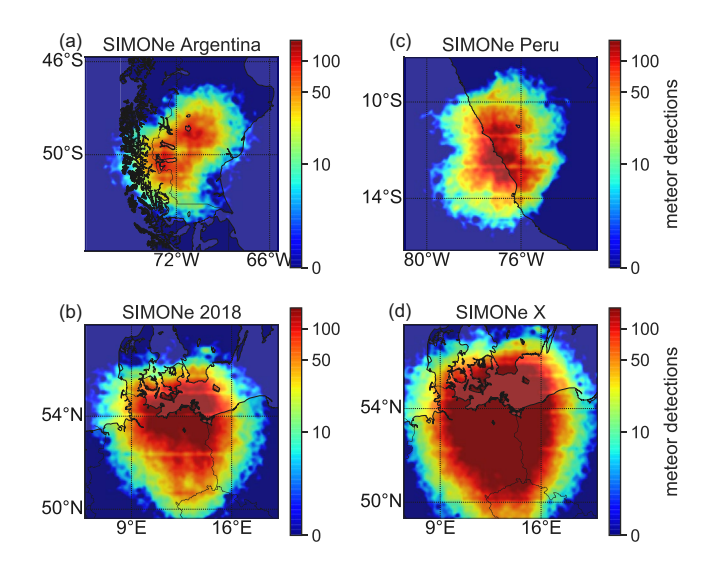


Figure 3. Density maps of 1 day of specular meteor observations at the existing SIMONe systems (SIMONe Argentina, SIMONe Peru, and SIMONe 2018) and SIMONe-X. Color bars represent the number of specular meteor detections in the \log_{10} scale.

We selected one arbitrary day from SIMONe 2018, SIMONe Peru, and SIMONe Argentina to conduct our analyses. For SIMONe 2018, we selected 5 November 2018. For Peru, it was 14 December 2019, and for Argentina, it was 19 February 2020. Figures 3a–3c show density maps of specular meteor counts on the selected days of SIMONe Argentina, SIMONe 2018, and Peru, respectively.

We modeled a pseudo-ideal SIMONe system called SIMONe-X based on the SIMONe 2018 geometry to create a more extensive system. Here, we used three independent days of sampling from SIMONe 2018 but translated the locations of meteors and radar links. In SIMONe-X, we used the data from November 5, 6, and 7, 2018 from SIMONe 2018. The meteors and antenna locations on November 5 stayed the same; however, the data from November 6 was translated by 0.5° north in latitude and 1.5° east in longitude. Data from November 7 was translated by 1.5° south in latitude and 0.5° east in longitude. In the SIMONe-X pseudo virtual system, we merged these three days of data into one day with 42 (14×3) meteor radar links and close to four-hundred thousand meteors per day. The purpose of creating such a pseudo system was to check the validity of our methods. The density map of meteor counts for SIMONe-X is shown in Figure 3d. The sampling of the meteor counts in this figure is based on the data used for the analyses.

4. Methodology

4.1. Temporal Gradients

Monostatic SMRs use radio reflections from specular meteor plasma trails to estimate the mean wind components for a given time and altitude bin, assuming horizontal homogeneity (over an area of 300–500 km diameter). The observation from each meteor trail includes the Doppler velocity, location of the scattering point of the trail, time of occurrence, angle of arrival, and Bragg wave vector, determined by the radar frequency and the observing geometry (Hocking, Kelley et al., 2001). Chau et al. (2017) relaxed the assumption of the homogeneity of the horizontal wind by applying a gradient approach that allowed estimating mean wind components and horizontal gradient terms.

Our study expands the gradient approach by including the temporal gradients of the horizontal wind components in the estimation. In the following set of equations, horizontal winds are considered non-homogeneous by using a Taylor series expansion of the wind velocity vector, including spatial and temporal gradients of the horizontal wind components.

$$u(x, y, z, t) = u_0 + \frac{\partial u}{\partial x}(x - x_0) + \frac{\partial u}{\partial y}(y - y_0) + \frac{\partial u}{\partial z}(z - z_0) + \frac{\partial u}{\partial t}(t - t_0),$$

$$v(x, y, z, t) = v_0 + \frac{\partial v}{\partial x}(x - x_0) + \frac{\partial v}{\partial y}(y - y_0) + \frac{\partial v}{\partial z}(z - z_0) + \frac{\partial v}{\partial t}(t - t_0),$$

$$w(x, y, z, t) = w_0 + \frac{\partial w}{\partial x}(x - x_0) + \frac{\partial w}{\partial y}(y - y_0) + \frac{\partial w}{\partial z}(z - z_0) + \frac{\partial w}{\partial t}(t - t_0),$$

$$(1)$$

where u, v, and w are the zonal, meridional and vertical components of the wind vector. u_0 , v_0 , and w_0 denote the mean wind components inside the volume. $\frac{\partial u}{\partial x}$, $\frac{\partial u}{\partial y}$, $\frac{\partial u}{\partial z}$, $\frac{\partial u}{\partial y}$, $\frac{\partial v}{\partial z}$, $\frac{\partial v}{\partial y}$, $\frac{\partial v}{\partial z}$, $\frac{\partial w}{\partial y}$, $\frac{\partial w}{\partial z}$ and, $\frac{\partial w}{\partial z}$ are the derivatives of the horizontal and vertical wind with respect to zonal, meridional, vertical, and temporal directions. In our study, we have not fitted for gradients of w, that is, we assume $\left(\frac{\partial w}{\partial x}, \frac{\partial w}{\partial y}, \frac{\partial w}{\partial z}, \frac{\partial w}{\partial t}\right) = 0$. Hence here we are solving for only 11 unknown parameters.

In the case of multistatic SMRs, by combining sufficient meteor observations within a time and altitude bin inside the radar volume, one can estimate these mean wind components and gradient terms by solving N equations of the form (Hocking, Kelley et al., 2001),

$$\vec{u} \cdot \vec{k}_{Bi} = 2\pi f_{di} \tag{2}$$

CHARUVIL ASOKAN ET AL. 6 of 21



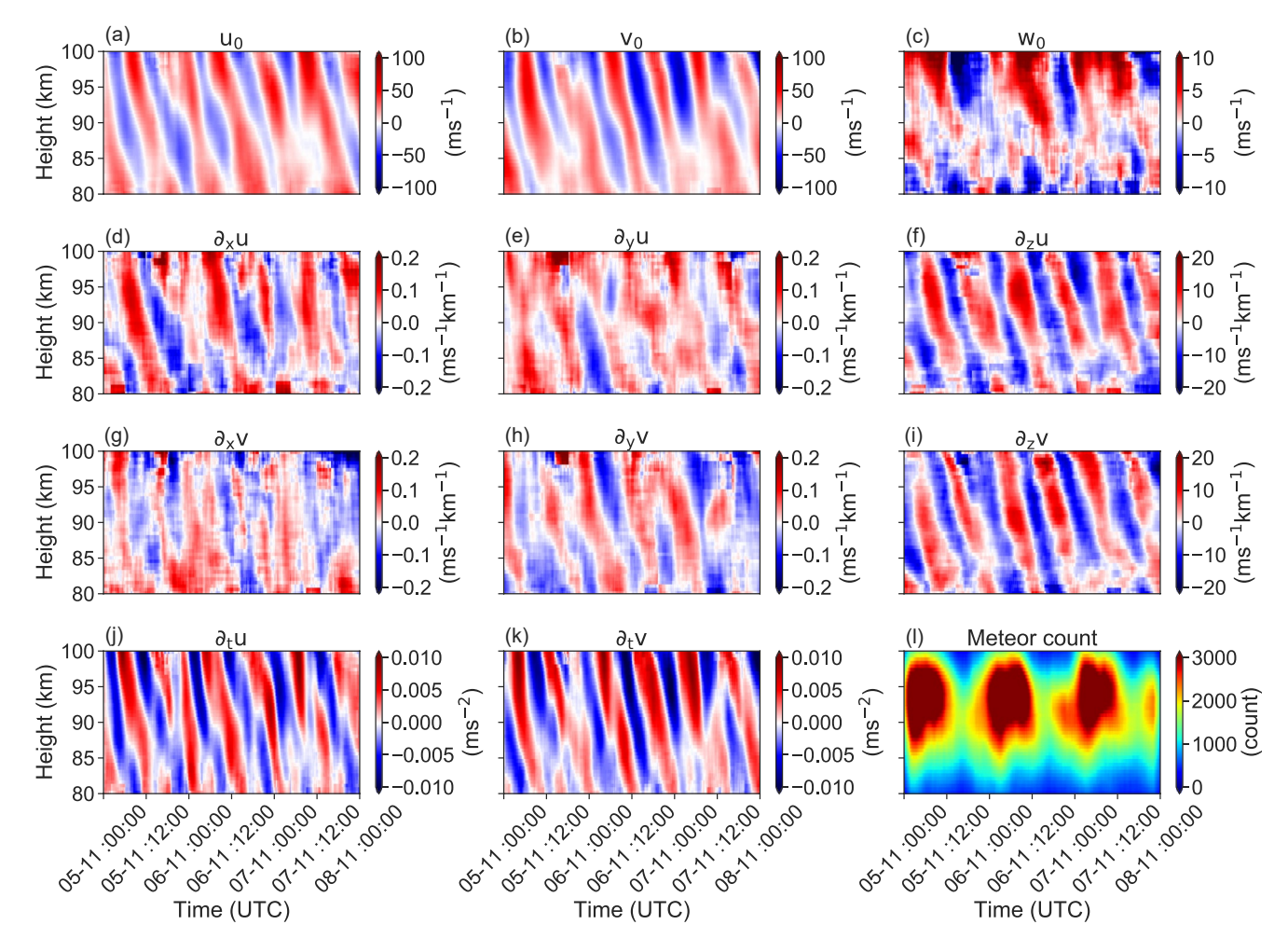


Figure 4. Mean winds and gradients estimates from November 5, 6, and 7 during SIMONe 2018. Panels (a) to (c) show the mean wind velocities, and panels (d) to (i) display the gradient terms of the horizontal wind components. Panel (l) shows the number of meteors used in the estimation.

where $\vec{u} = (u(x, y, z, t), v(x, y, z, t), w(x, y, z, t))$ is the wind vector and f_{di} , \vec{k}_{Bi} are the Doppler shift and Bragg wave vector of each meteor echo, respectively.

Figure 4 shows mean winds and gradients estimates from 3 days (November 5, 6, and 7) during SIMONe 2018 as an example of the updated gradient estimation technique. Figures 4a–4c display the mean wind velocities obtained from the estimation. Figures 4d–4i show the spatial gradient terms of the horizontal wind components. Figures 4j and 4k show the newly derived parameters, that is, $\partial_t u = \frac{\partial u}{\partial t}$ and $\partial_t v = \frac{\partial v}{\partial t}$. Figure 4l indicates the number of specular meteors. We estimated these components using 4 hour-4 km time-altitude bins within the selected radar observing volume (radius of 200 km).

4.2. Virtual Multistatic Meteor Radar (VMMR)

Due to the lack of independent spatially resolved winds in the MLT region, it is almost impossible to validate the parameters measured by ground-based instruments. Although some global circulation models correlate with ground-based instruments in a climatological sense, the daily variability and extreme events are not well represented (e.g., Conte et al., 2018; Davis et al., 2013). Since each ground-based instrument measures different parameters at different local volumes, direct verification is also tricky.

The idea of a VMMR network based on a high-resolution model thus gains importance in validating the methodology used to estimate the parameters observed by multistatic SMRs. Here, we are considering the model

CHARUVIL ASOKAN ET AL. 7 of 21



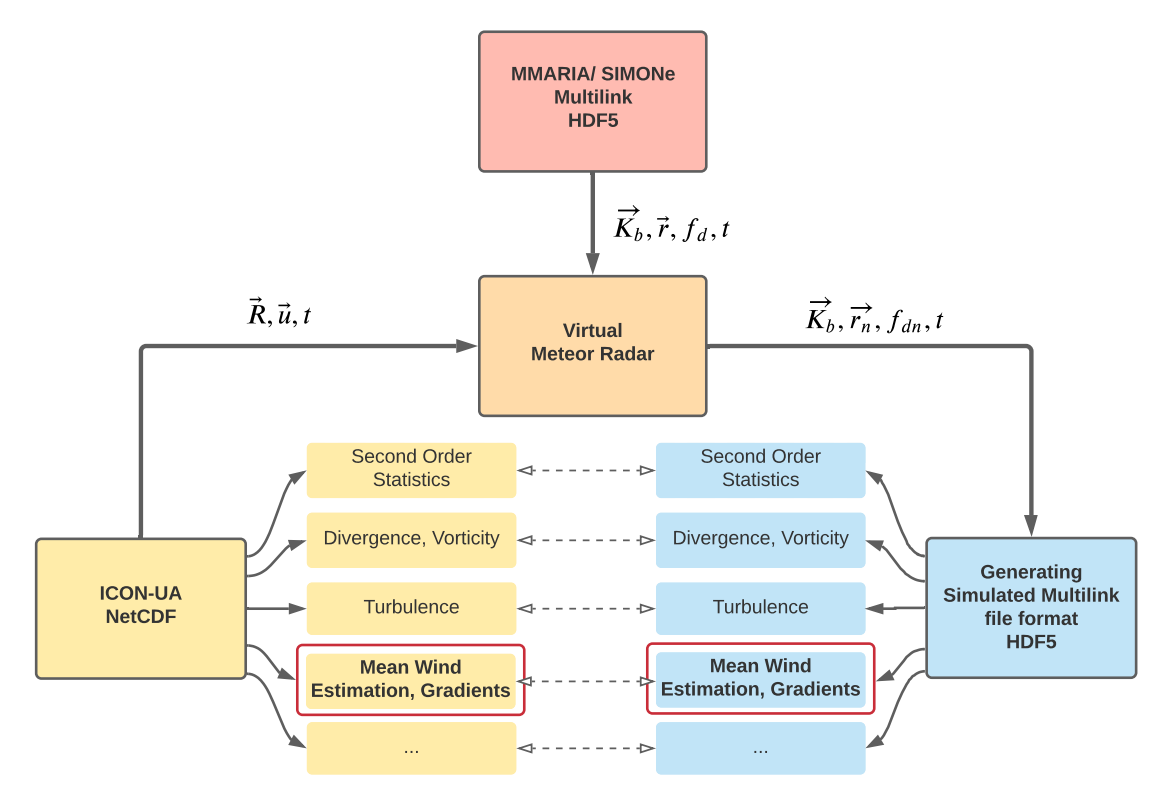


Figure 5. Block diagram summarizing the Virtual meteor radar network.

atmosphere simulated by UA-ICON as our pseudo atmosphere. Then, based on the SIMONe geometries and meteor samplings from each system, we probe the UA-ICON atmosphere to measure the parameters in a way in which multistatic SMRs conduct actual measurements. It is to be noted that, in the current study, we do not compare the results from the UA-ICON and SIMONe systems. Instead, we are creating a tool VMMR to validate the methods used by the multistatic SMRs to estimate winds and gradients. This tool can be extended to validate all the analyses done by meteor radar observations in the future. A block diagram of our VMMR is shown in Figure 5.

UA-ICON provides the zonal (u), meridional (v), and vertical (w) wind component values at each grid position in space and time. However, the SIMONe meteor data contains one-dimensional projections (Doppler shift) of the velocity field and other parameters also depending on the location of meteors, such as Bragg wave vector and angle of arrival. Since the meteor measurements are sparse and randomly measured in nature, they have an irregular sampling structure in space and time.

First, we place the four SIMONe geometries (SIMONe 2018, SIMONe Peru, SIMONe Argentina, and SIMONe-X) onto the UA-ICON model base. A visualization example of one of such placements can be seen in Figures 6a–6c. Figures 6a–6c displays a time frame (5 min) at 90 km altitude in the latitude-longitude cut data of u, v, and w from the UA-ICON model. The small gray stars in these plots show meteors' locations within 5 min from SIMONe 2018. Similarly, Figures 6d–6f show the average of such time frames for 30 min, and the gray stars correspond to the meteors observed in 30 min.

After placing the SIMONe geometries on the UA-ICON data, the next step is to find the spatially and temporally closest grid position in the UA-ICON for each meteor observation. Then, we use the original Bragg vectors from the observations and the UA-ICON wind velocity vector (u, v, w) that correspond to these grid points to calculate a new set of simulated Doppler velocities using Equation 2. As shown in the block diagram in Figure 5, the system thus generates VMMR simulated Doppler velocities corresponding to each meteor observation.

To include the location uncertainties in the simulated data, we performed the following procedure. We used the wind vector from the closest grid point to estimate the simulated Doppler velocity but projected on the virtual

CHARUVIL ASOKAN ET AL. 8 of 21



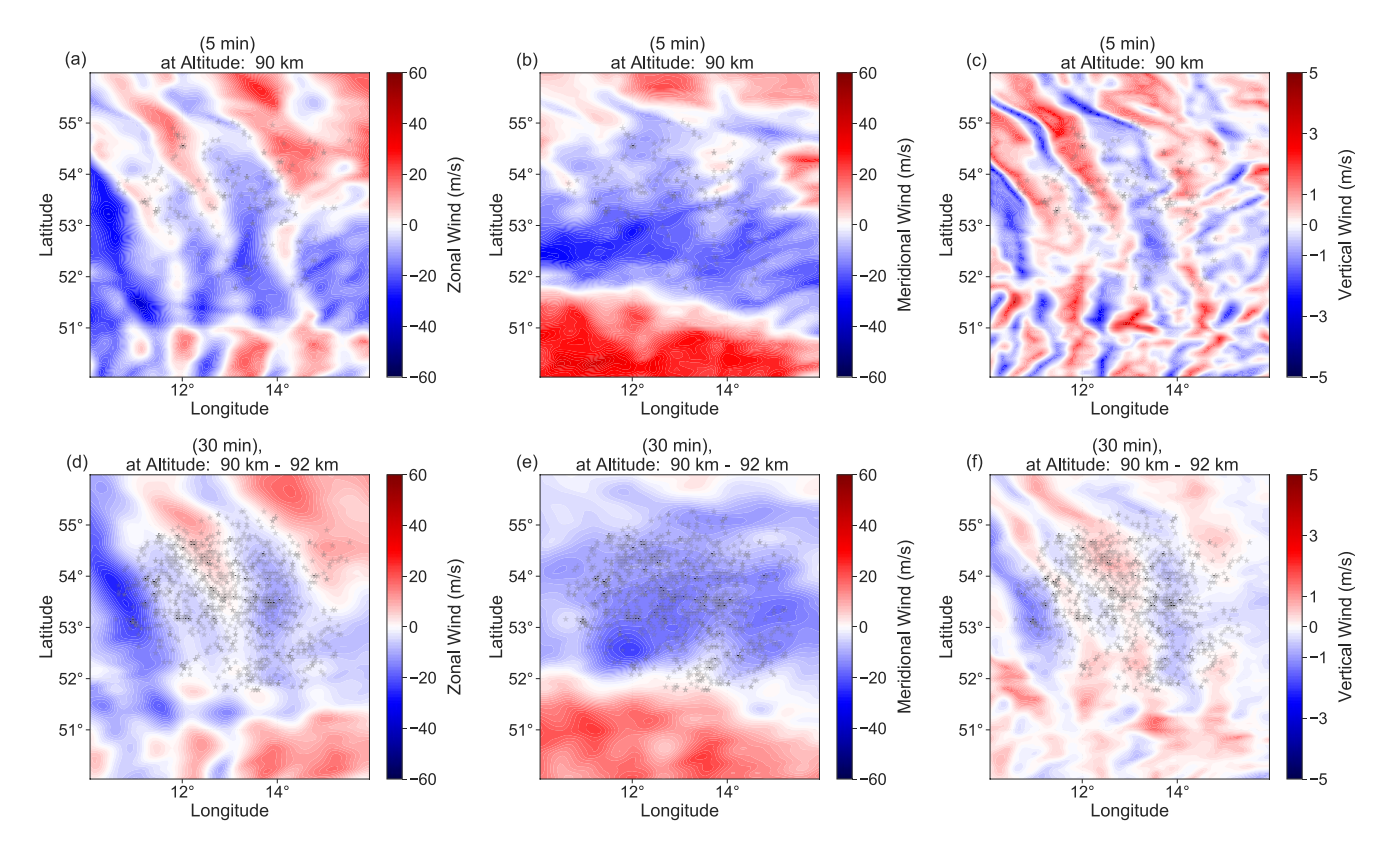


Figure 6. (a–c) show the latitude-longitude section of zonal, meridional and vertical wind components at 90 km (vertical level spacing = 600 m) altitude and a single time-frame (resolution = 5 min) from the UA-ICON. (d–f) are similar to (a–c), but these figures are obtained after averaging the winds for 30 min and 2 km in altitude (90–92 km). Small gray stars in the figures correspond to the location of observed meteors for 5 min (a–c) and 30 min (d–f) time windows.

radar's location with a Bragg vector that corresponds to the actual meteor observation. This condition creates a maximum uncertainty of ± 2.5 km (5 km horizontal grid spacing) in latitude and longitudinal directions and ± 300 m (600 m vertical level spacing in UA-ICON) in altitude direction. We also added uncertainty in altitude related to the elevation angle of the meteor detection. The lower elevation angle detections from SMRs show a higher error in the location estimation, especially in the altitude estimation (Clahsen, 2018).

Therefore, we added a Δh term to the existing heights from the measurements based on the following equations.

$$\Delta h = \begin{cases} 500 \cdot \xi, & \text{if } \theta \le 35^{\circ} \\ ae^{b\theta} \cdot \xi, & \text{if } \theta > 35^{\circ} \end{cases}$$
(3)

$$h' = h + \Delta h,\tag{4}$$

where θ is the elevation angle, h is the existing altitude from SMR observations, and h' is the new simulated altitude used in the VMMR system corresponding to each measurement. The terms a and b are calculated based on the exponential function $f(\theta) = ae^{b\theta}$ in Equation 3, with limits $f(35^\circ) = 500$ m and $f(65^\circ) = 2000$ m. The term ξ in Equation 3 corresponds to the random number multiplier based on the standard normal distribution.

The simulated VMMR data structure is identical to the actual multistatic SMR observation data structure. This allows us to carry out all meteor radar analyses, including mean winds and gradient estimation, divergence, vorticity estimation and, to study second-order statistics (Vierinen et al., 2019). Since high-resolution model data from UA-ICON allow us to determine these parameters, most of the SMRs analysis techniques could be

CHARUVIL ASOKAN ET AL. 9 of 21



potentially validated. In this paper, our focus is on validating the mean wind and gradient estimation techniques for multistatic SMRs.

4.3. Validation Through Performance Metrics

In order to get a general overview of the performance of the SIMONe analysis through the virtual meteor radar technique, we examine the performance metrics calculated for the estimated parameters. We use correlation coefficient (CC), mean-error (ME) and, root-mean-square-error (RMSE) to analyze the performance of our technique on the mean wind and gradient estimation.

In order to compare the parameters obtained from the VMMR and UA-ICON, we carried out a similar averaging for both data. The mean winds and gradients from the simulated VMMR data were estimated by least-square fitting the Doppler velocities to mean winds and gradients using different time and altitude bins. In these calculations (Equations 1 and 2), we used simulated measurements within a 200 km radius.

The UA-ICON model data have zonal, meridional, and vertical velocities at each grid point. We estimated the mean winds and gradients from the gridded UA-ICON data utilizing the similar averaging used in the VMMR analysis.

It should be noted that the mean winds and gradients obtained from the UA-ICON utilize the entire grid-points within the defined volume. For example, in the case of 1 hr- 2 km bin averaging, we consider all the gridpoints within a disc of radius 200 and 2 km thickness and a time window of 1 hr. However, the virtual meteor data obtained using the UA-ICON uses only the sparse sampling of meteors observed within the same volume and time window to estimate the mean winds and gradients. These estimated quantities obtained from UA-ICON model data and simulated virtual radar data are then validated using performance metrics (see above).

5. Results

5.1. Validation Statistics

We estimated the mean winds and gradients using two different averaging kernels: 1 hr - 2 km and 4 hr-4 km time-altitude bins from both the simulated data from VMMR and UA-ICON model data to validate the estimation techniques. Their performance metrics are shown in Figure 7. Figures 7a and 7d correspond to the CC between the VMMR simulated and UA-ICON data for the two datasets, respectively. In all graphics of Figure 7, the x-axis labels correspond to mean zonal wind (u), $\partial_x u = \frac{\partial u}{\partial x}$, $\partial_y u = \frac{\partial u}{\partial y}$, $\partial_z u = \frac{\partial u}{\partial z}$, $\partial_t u = \frac{\partial u}{\partial t}$, mean meridional wind (v), $\partial_x v = \frac{\partial v}{\partial x}$, $\partial_y v = \frac{\partial v}{\partial y}$, $\partial_z v = \frac{\partial v}{\partial z}$, $\partial_t v = \frac{\partial v}{\partial t}$ and, mean vertical wind (w). The four different lines in each plot correspond to each SIMONe geometry used for the VMMR network simulation. Red, blue, green and black correspond to SIMONe Peru, SIMONe Argentina, SIMONe 2018 and SIMONe-X geometry results, respectively.

In Figures 7a and 7d, the CC between the VMMR simulated and model data show good agreement except for vertical velocity estimates. The mean wind components (u and v) estimated from simulated virtual radar data show excellent agreement with the UA-ICON data, regardless of the SIMONE geometries used in the virtual radar system. In the gradient estimation, the geometries with a larger number of independent measurements such as SIMONe 2018 and SIMONe-X deliver optimal results. The SIMONe Peru and Argentina geometries show a good correlation, but not as good as the other two geometries. In Figure 7, we normalized the values of the ME and RMSE using the corresponding standard deviation (σ_{ICON}) from UA-ICON model data. It is carried out to normalize the units of mean winds and gradients. These values are included as a Table S1 in Supporting Information S1. In Figures 7b, 7c, 7e, and 7f, the normalized ME and RMSE show similar statistics as in the case of CC. Except for the vertical velocity estimates, the mean wind components show good agreement, and gradient estimation shows good agreement in the case of SIMONe 2018 and SIMONe-X systems and fair agreement in the case of SIMONe Peru and Argentina.

CHARUVIL ASOKAN ET AL. 10 of 21



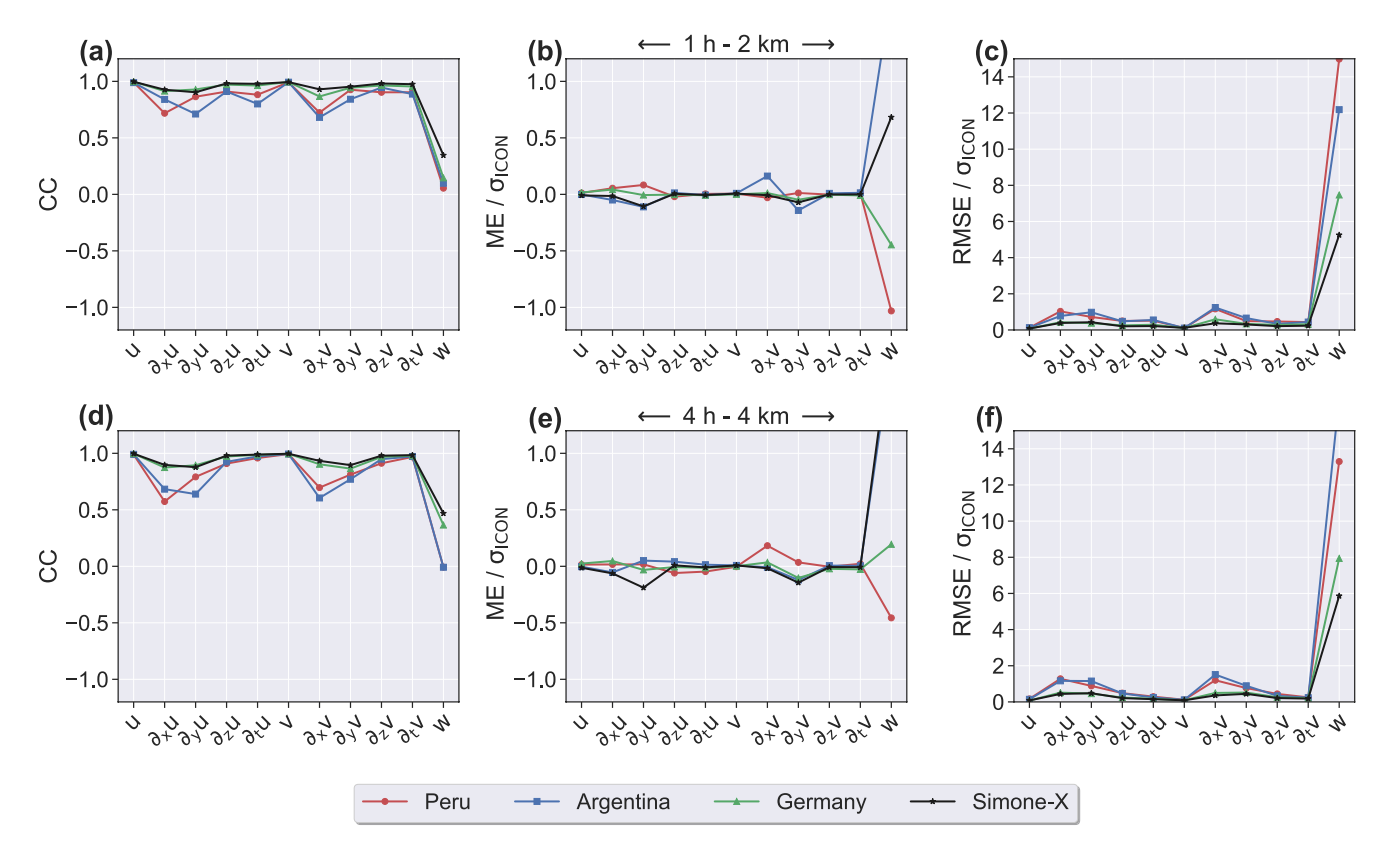


Figure 7. The figure shows the performance metrics, such as correlation coefficient (a), (d), mean-error (b), (e), and root-mean-square-error (c), (f) used in the study to validate the specular meteor radar gradient approach. The top and bottom rows show the validation of mean winds and gradients estimated using 1 hr - 2 km and 4 hr-4 km time-altitude bins, respectively. Red corresponds to SIMONe Peru geometry, blue to Argentina, green to SIMONe 2018 and the black line corresponds to the SIMONe-X geometry results.

5.2. Introduction of Large Scale Vertical Velocities to UA-ICON

From the analyses, we found that the estimated mean vertical velocity is significantly larger than the mean vertical velocity values from the UA-ICON model (Figure 8b). However, the VMMR estimates did not show the tidal features observed in actual SIMONe data from Peru, Argentina, and SIMONe 2018 (Figure 1). This motivated us to create hypothetical situations by inducing 24-hr period waves with 40 km vertical wavelengths into the UA-ICON model vertical velocity output. We treated the horizontal wavelength of these induced waves as essentially infinite. Here, "inducing" means adding the wave perturbations to the existing wind fields. Then, we performed the virtual network technique on the tide-induced UA-ICON data and created new sets of simulated radar data for each geometry. Namely, we redo the VMMR data generation but adding large-scale vertical velocity waves with horizontal scales greater than the radar observing volume. Results from this analysis using 1 hr–2 km averaging kernels are shown in Figure 8.

Figures 8a and 8b show the actual vertical velocity averaged from the UA-ICON model and the estimated vertical velocity using virtual SIMONe 2018, respectively (to see the variance of vertical velocities from UA-ICON refer to Figure 9a). Here, the estimated vertical velocities do not agree with those from the model data. Figure 8c shows the first test after setting vertical velocities equal to zero in the UA-ICON data, and Figure 8d shows the corresponding estimates of the vertical velocity using the virtual system. Surprisingly, Figures 8b and 8d look qualitatively similar even though the model vertical velocity has been set to zero in all grid points.

Further tests on the vertical velocity consisted of introducing 24-hr tidal features into the vertical velocities. Figure 8e shows the test result after introducing a 2 m/s tidal structure into the UA-ICON model, and Figure 8f shows the corresponding estimate from the virtual system. Figures 8g and 8h show a similar test with the addition of a 5 m/s daily tidal structure to the UA-ICON model. To check the efficiency of the tide-induced tests,

CHARUVIL ASOKAN ET AL. 11 of 21

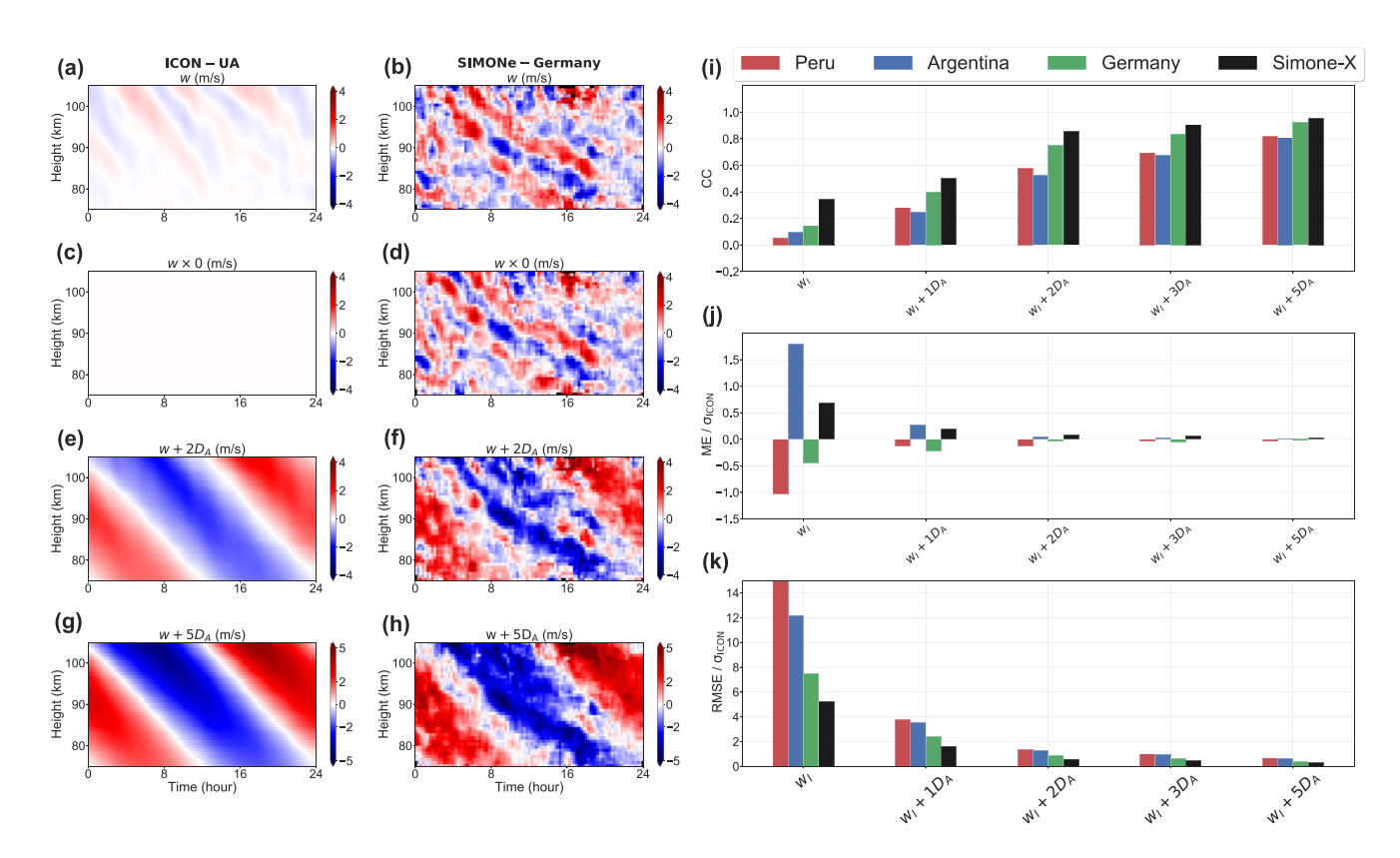


Figure 8. Results from the virtual network technique on the tide-induced UA-ICON data and subsequent Virtual radar data. Panels (a) and (b) show the actual vertical velocity averaged from the UA-ICON model and the estimated vertical velocity using virtual SIMONe 2018, respectively. Panel (c) shows the results after applying zero vertical velocities to the UA-ICON data, and (d) shows the corresponding estimate of vertical velocity using the virtual system. Panels (e)—(f) and (g)—(h) show test results from the induction of 2 m/s and 5 m/s tidal structures to the UA-ICON model and their corresponding estimates using the VMMR, respectively. Panels (i) (j), and (k) show correlation coefficient, root-mean-square-error, and mean-error values for different tide-induced tests, respectively. The *x*-axis labels to the bar plots in (i), (j), and (k) depict the tide-induced tests with different amplitudes from 1 m/s to 5 m/s. Colors in the bar plots correspond to each of the SIMONe geometries used in the analyses; red - SIMONe Peru, blue - SIMONe Argentina, green - SIMONe Germany, black - SIMONe-X.

we utilized the performance metrics. Figures 8i–8k show CC, RMSE, and ME values for different tide-induced tests, respectively. The *x*-axis labels of the bar plots in these figures depict the tide-induced tests with different amplitudes from 1 m/s to 5 m/s. Colors in the bar plots correspond to each of the SIMONe geometries used in the analyses; red - SIMONe Peru, blue - SIMONe Argentina, green - SIMONe Germany, black - SIMONe-X. From Figure 8, it is clear that as the amplitude of a dominant tidal structure increases, the meteor radar systems can estimate them more accurately.

6. Discussion

6.1. Mean Horizontal Winds and Gradients

This paper presents a validation study of multistatic SMRs for mean winds and gradients in the MLT region. The mean zonal and meridional winds estimated from virtual SIMONe systems are in excellent agreement with the winds from UA-ICON model data. The performance metrics used to validate the mean zonal and meridional wind estimates (Figure 7) show a good correlation, regardless of the SIMONe geometries used in the virtual radar system. Two different averaging kernels used in the analyses in Figure 7 (i.e., 1 hr- 2 km and 4 hr- 4 km) show similar results, which displays the consistency of the results.

The validation of horizontal wind estimates is expected to be good since the sampling geometry and viewing angle of SMRs favor the Bragg vector components in the horizontal direction. These products are used to study tides, planetary waves, and gravity wave activity in the MLT region (e.g., Conte et al., 2017; Murphy et al., 2006;

CHARUVIL ASOKAN ET AL. 12 of 21



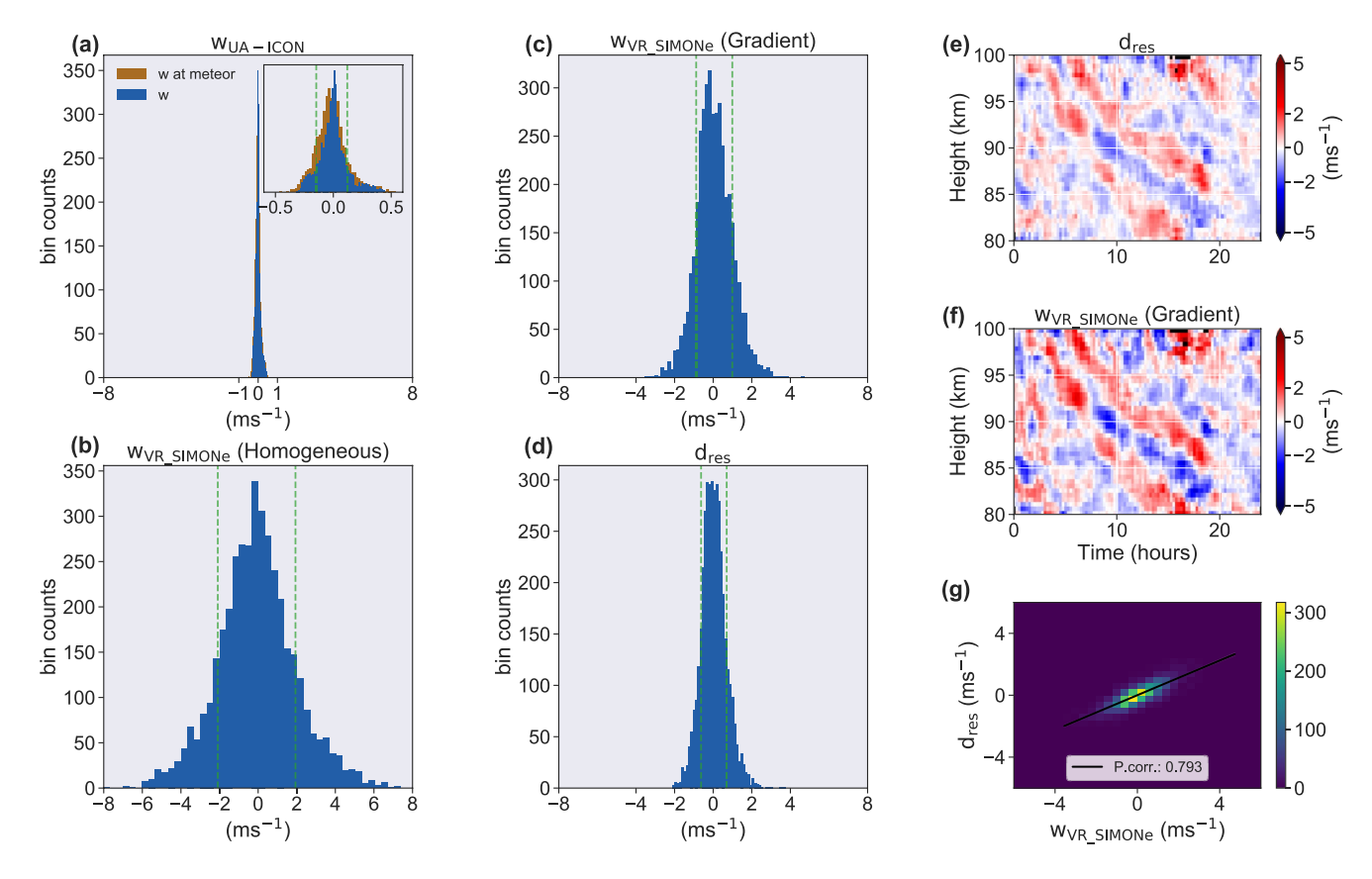


Figure 9. Panel (a) shows the histogram of vertical velocities from the UA-ICON model. Blue colored histogram in (a) corresponds to data obtained by the similar averaging used in the meteor radar analysis. The orange-colored histogram in (a) shows the data obtained by selecting only the grid points in UA-ICON close to the meteor positions. Panels (b) and (c) show the histograms of vertical velocities estimated using the homogeneous and gradient approach from VMMR respectively. Panel (d) shows the histogram of residual Doppler estimated using Equation 9. Panels (e) and (f) show the altitude-time plots of the residual Doppler and the vertical velocity, respectively that were estimated using the gradient approach. Finally, panel (g) shows the correlation between the vertical velocity estimate and the residual Doppler.

Sandford et al., 2006). SMR horizontal wind measurements are also used for long-term studies of the MLT region (e.g., Jaen et al., 2021; Wilhelm et al., 2019). Previous comparative studies between meteor radars and other ground-based instruments have also shown agreement. For example, Liu et al. (2002); Franke (2005), and recently Kishore Kumar et al. (2018) showed that the horizontal winds estimated with lidars and meteor radars are well correlated. Many studies have also compared meteor radars with medium frequency radars and Fabry-Perot Interferometers, finding good agreement in the horizontal wind estimates (e.g., Cervera & Reid, 1995; Jacobi et al., 2009; Jiang et al., 2012; Wilhelm et al., 2017; Yu et al., 2016).

Figure 7 also shows fair agreement in the estimation of the gradient terms. Gradient terms of the wind fields help to study the horizontal divergence and relative vorticity fields in the MLT region (Chau et al., 2017; Laskar et al., 2017). Our validation study suggests that SIMONe 2018 and the pseudo-ideal - SIMONe-X show a better correlation with the UA-ICON model data than the SIMONe Argentina and Peru systems, as expected given their larger number of counts and higher viewing angle diversity. SIMONe Argentina and Peru consist of 5 SMR links each, and SIMONe Germany during the campaign 2018 had 14 radar links. The pseudo-SIMONe-X has 42 radar links. As the number of links increases, the number of independent meteor samples will also increase and produce better estimates of gradients. Our validation study on the gradient estimation thus confirms the importance of creating multistatic SMRs with a larger number of radar links. More extensive systems will improve the quality of the gradient estimation and improve the possibilities of further studies with these quantities. It shows that the coverage beyond SIMONe 2018 in an approximately 400 km diameter space does not provide further returns in the case of mean winds and gradient estimations. However, we are not aware that this impression holds in the

CHARUVIL ASOKAN ET AL. 13 of 21



case of second-order statistics studies such as mesoscale momentum flux, power spectral, and structure-function studies (e.g., Charuvil Asokan et al., 2021; Conte et al., 2021; Vierinen et al., 2019).

6.2. Vertical Velocity Estimation

The primary motivation of this study is to understand the unprecedented mean vertical velocity estimates from the SIMONe systems mentioned above and other multistatic SMRs. We found that the vertical velocity estimates have unexpected large amplitudes and show tidal features. From our VMMR results, the estimated horizontal winds and gradients showed a clear correlation with the model data; however, vertical velocity estimates did not show a good correlation.

The estimated vertical velocities from our virtual radar analysis show a variability of ± 1 –2 m/s. However, this analysis does not represent the tidal features observed in the actual SIMONe systems data, particularly above 95 km. One possible reason for the small variability observed in the SIMONe analysis is the contamination from small horizontal inhomogeneities in the horizontal wind.

In our current wind estimation technique, we consider each of the horizontal components as mean wind components and their gradient terms in space and time as described in Equation 1. By separating the horizontal wind between a mean value and a zero-mean perturbation, Equation 1 is rewritten as:

$$u(x, y, z, t) = u_0 + u'$$

$$v(x, y, z, t) = v_0 + v'$$

$$w(x, y, z, t) = w_0,$$
(5)

where u_0 , v_0 , w_0 are the mean components and u' and v' are the components that include all the gradient terms in zonal and meridional velocities as described in Equation 1.

From Equation 2, then we can elaborate,

$$2\pi f_d = \vec{u} \cdot \vec{k_B} = (u_0 + u') k_x + (v_0 + v') k_y + w_0 k_z \tag{6}$$

In the ideal case, if we rearrange Equation 6, we should get,

$$2\pi f_d - (u_0 + u') k_x - (v_0 + v') k_y - w_0 k_z = 0$$
(7)

If we assume $w_0 = 0$, then we can reduce Equation 7 to,

$$2\pi f_d - (u_0 + u') k_x - (v_0 + v') k_y = 0$$
(8)

However, the virtual radar analysis based on the UA-ICON model suggests a different result. In our analysis, Equation 8 does not equate to zero but gives a residual value. We call the latter residual Doppler (d_{res}). Our speculation of vertical velocity being the result of contamination from horizontal components is due to the presence of a residual Doppler.

Figure 9 shows the comprehensive outlook of this assumption. Figure 9a shows the histogram of vertical velocities from the UA-ICON model. These values are obtained in two ways. First by averaging as in the meteor radar analysis, that is, 1 hr- 2 km time-altitude bins over a region of 200 km horizontal radius from the model output. This is shown as the blue-colored histogram in Figure 9a. The orange-colored histogram denotes the second method in Figure 9a, which shows a similar averaging, without selecting every grid point from the model in the averaging volume, but taking only the grid points close to the meteor positions from SIMONe 2018 geometry. We carried out this special averaging to check if the meteor sampling creates any further uncertainty in the observation. However, both histograms from Figure 9a show similar mean and variance.

Figure 9a shows that the model data gives a close to zero mean and ± 0.13 m/s standard deviation for the vertical winds when we use the similar averaging used in the meteor radar analysis. To estimate the winds from meteor radars, we use two methods. The first method is called homogeneous method, where we least-square fit only the

CHARUVIL ASOKAN ET AL. 14 of 21



mean wind components, namely, u_0 , v_0 , and w_0 . The second approach is called the gradient method, where we fit the mean wind components and the gradient terms as described in Equations 1 and 2. Chau et al. (2017) showed the difference between these methods. They concluded that the gradient approach is suitable for a better estimate of mean winds and showed the potential of the estimated gradient terms in deriving physical quantities such as horizontal divergence, relative vorticity, shearing deformation, and stretching of the wind field. The only difference of the gradient approach between our study and Chau et al., 2017 is the added temporal gradients described in Section 4.1. Figures 9b and 9c show the histogram of vertical velocities estimated using the homogeneous and gradient approach on the simulated meteor radar (SIMONe 2018 geometry) data based on the UA-ICON model. Vertical velocity estimates from the homogeneous method give a mean of -0.07 m/s and a standard deviation of 2.01 m/s. The estimates from the gradient method give a mean of 0.05 m/s and a standard deviation of 0.94 m/s. Although the gradient method reduces the variance of the estimates significantly compared to the homogeneous approach, they are not close to the actual UA-ICON data shown in Figure 9a. Here we compare the values of the UA-ICON data with the VMMR-based SIMONe results. It should be pointed out that we do not compare the velocity values of UA-ICON with the real SIMONe systems, as we do not consider the UA-ICON model as the single standard for comparison.

By our definition and using Equation 7, we can write the residual Doppler (d_{res}) as,

$$d_{res} \approx 2\pi f_d - (u_0 + u') k_x - (v_0 + v') k_y \approx w_0 k_z$$
(9)

Using Equation 9, we estimated the d_{res} , and the histogram from its values is shown in Figure 9d. To make the d_{res} units to m/s, we divided them with the magnitude of \vec{k}_B . The mean value of the residual Doppler is 0.03 m/s, and the standard deviation is 0.66 m/s. Figures 9e and 9f show the altitude-time plots of the residual Doppler and the vertical velocity, respectively, that were estimated using the gradient approach. From Figure 9c through 9f, we can see a qualitative similarity between the residual Doppler and the estimates of vertical velocity. We find a CC of 0.79 between these quantities as shown in Figure 9g.

This analysis gives rise to our speculation about the vertical velocity estimates. We think that this residual Doppler is the result of contamination from horizontal components to the vertical velocity estimates. It suggests that the estimated vertical velocity in our analysis is a combination of actual vertical velocity and horizontal contamination. When we fit the mean winds and gradient terms as per Equations 1 and 2, we leave out the small-scale fluctuations within the time-altitude-horizontal bin. These small-scale fluctuations are velocity fluctuations with horizontal scales less than 400 km that are not captured due to the horizontal averaging used in our wind estimation methods. The introduction of gradient terms reduces the biases in our estimation. However, it is not enough to estimate mean vertical winds if the actual mean vertical wind is less than $\pm 1-2$ m/s.

In Equation 5, the primed quantities constitute the gradient terms, and the non-primed are the mean wind components. However, it is clear from our results that the small-scale fluctuations in the zonal and meridional winds are not included in Equation 5. If we modify Equation 5, we can write,

$$u(x, y, z, t) = u_0 + u' + u^{\alpha}$$

$$v(x, y, z, t) = v_0 + v' + v^{\alpha}$$

$$w(x, y, z, t) = w_0,$$
(10)

where u^{α} and v^{α} are the quantities that represent the small-scale fluctuations in the zonal and meridional wind that are not fitted in the gradient approach.

These underrepresented quantities are the reason for the variability of ± 1 –2 m/s in the estimates of the vertical velocities. Therefore, all estimates of vertical velocities from the SIMONe systems using the gradient approach with a variability of less than ± 2 m/s should be treated with extra caution. Due to the smoothing inherent to the model results, these results should be treated as lower bounds to the error incurred using real data.

Recent attempts by Chau, Urco, et al. (2021); Stober et al. (2018, 2021), and Volz et al. (2021) independently described different methods for estimating horizontally resolved winds at the MLT heights with SMRs. These works take into account the inhomogeneity of horizontal winds, which helps to break down winds horizontally

CHARUVIL ASOKAN ET AL. 15 of 21



in structures which are a few kilometers in size. We believe that such efforts can help to understand the contamination of vertical winds by horizontal inhomogeneities in the gradient approach of multistatic SMRs in general and not just SIMONe.

6.3. Vertical Velocity Estimation: Tidal-Like Features

In our VMMR analysis using the model data, we find that the small-scale structures of the order of $\pm 1-2$ m/s are due to horizontal wind contamination. However, this result does not explain the tidal-like features found in the actual SIMONe data from Germany, Peru, and Argentina (Figure 1). These tidal-like features are more significant at altitudes around and above 95 km (Figure 2) and sometimes reach more than 5 m/s in amplitude. Since we used various SIMONe geometries in our VMMR, we can claim that these tidal patterns are not the result of sampling or geometry errors.

Due to the lack of independent observations of vertical winds, it is challenging to assert geophysical implications to the unexpected mean values and tidal features observed in our SIMONe systems. As stated before, most of the SMR studies did not fit for vertical winds. They consider the vertical velocity to be zero. However, we found that high tidal mean amplitudes in the vertical winds from monostatic SMR were previously reported by Chang et al. (1999). They observed a diurnal amplitude of 10–15 m/s, which maximizes at midnight across all heights using a narrow-beam meteor radar at Christmas Island. Chang et al. (1999) speculated that meteor trail scattering is a possible reason for the strong diurnal amplitude observed in Christmas Island. Some of the later studies acknowledged the issue as speculation. However, they chose to neglect these influences since most SMRs estimate winds only below 100 km (Hocking, 2001). The current general circulation models also suggest that synoptic-scale vertical winds are in the order of a few cm/s (Smith, 2012), although most assume an atmosphere in hydrostatic equilibrium.

To find the possible reasons for the observed tidal features in vertical velocity estimates, we analyzed the actual SIMONe data. One hypothesis is the influence of ion drag on the meteor trail scattering. According to the ion momentum equation, there is a vertical drift in the presence of a zonal wind. This effect is maximized at about 130 km altitude and gradually weakens at lower altitudes due to the stronger coupling of ions to neutrals. A detailed description of the mechanism can be found in Haldoupis (2011). According to Haldoupis (2011), the vertical ion drift can be up to 2 m/s at 100 km altitude. We know that the trail scattering is associated with the electrons; however, they are strongly coupled to the ions. Our hypothesis suggests that electron mean velocity will track primarily the ions, which are coupled strongly to the neutrals but deviate slightly due to Lorentz force. According to this assumption, we would expect the following behaviors: If the neutral wind is westward, there will be a downward ion velocity. If the neutral wind is eastward, there will be an upward ion velocity. If plasma motion is the mechanism, we should expect a correlation between zonal winds and vertical winds. For example, if there is a diurnal pattern in the zonal wind, there could be a diurnal pattern in the vertical wind estimates.

A simple analysis based on this hypothesis could not explain the diurnal-like pattern in the vertical wind. The estimated vertical components from our three systems did not show a correlation with horizontal components (not shown here). Also, as stated before, zonal winds in Germany during the SIMONe 2018 campaign had a clear semi-diurnal pattern (mid-latitude phenomena); however, the vertical wind had a diurnal pattern. Although we failed to find the answer from the hypothesis mentioned above, some missing aspects of the scattering at these altitudes may affect the vertical velocity estimates and should be studied in the future.

We carried out further studies to see the dependence of estimated vertical winds on the geomagnetic activity and latitudinal dependence. As shown in Figures 1 and 2, tidal-like structures in vertical winds are present in Peru (\sim 12°S), Germany (\sim 54°N), and Argentina (\sim 50°S). Hence, we cannot see a latitudinal dependence in the estimates. Preliminary analysis with geomagnetic indices such as Kp (Matzka, Stolle, et al., 2021) and Hpo (Matzka, Bronkalla, et al., 2021) did not show any significant correlation with the vertical velocity estimates.

To our understanding of the MLT dynamics, such values and tidal-like features in the mean vertical estimates would mean that large-scale horizontal structures would have a few meters per second vertical motions. It would also create a considerable change in the temperature of the lower thermosphere region, which should be observed by satellites such as Sounding of the Atmosphere using Broadband Emission Radiometry (SABER). However,

CHARUVIL ASOKAN ET AL. 16 of 21



preliminary analysis based on the SABER satellite did not give any evidence to support this motion (Vargas et al., 2021).

The next problem we address in our analysis is to see if multistatic SMR systems can detect large-scale waves in the vertical wind if they are present in the MLT region. As shown in Section 5.2, to test the extent of our systems, we introduced large-scale waves to the vertical component of the model data. In each iteration, we gradually increased the amplitude of 24-hr period waves. As we reached an amplitude of 2 m/s, we began to reproduce the features using our virtual SIMONe systems (Figure 9). This analysis substantiated our preliminary study (Section 6.1) using the VMMR by stating that the variability less than ± 2 m/s is highly speculative due to the horizontal contamination. However, if there is a persistent large-scale wave present in the MLT with an amplitude of more than 2 m/s, the SIMONe systems should be able to capture them effectively.

To test the possibility of observing large-scale waves in the vertical wind in the MLT using SMRs, we introduced diurnal tides in the UA-ICON vertical wind with amplitudes up to 5 m/s. However, these added waves are not based on any realistic atmospheric condition that we are aware of; instead, they are introduced only to see the capability of multistatic SMRs to detect large-scale waves in the vertical wind if they are present in the MLT. Thus, we are not using this test to give geophysical implications to the tidal-like features observed in the actual SIMONe observations in Argentina, Germany, and Peru.

From our preliminary analyses on the tidal-like features on the vertical wind in the actual data, we could not find a connection to any geophysical phenomena that could be a potential reason. However, since the observed values are not expected, we speculate that there might be some missing aspects of the scattering at these altitudes that might affect mainly the vertical velocities. Therefore, understanding these tidal features and mean values will require further investigations based mainly on the scattering mechanisms at altitudes above 90 km and non-hydrostatic general circulation models with higher resolution. We would also propose multi-instrumental campaigns to understand our results of large-scale waves observed in the vertical velocity from multistatic SMR systems.

7. Conclusions

In this work, we present a validation study of mean winds and gradient estimation analysis of multistatic SMRs. Our study is motivated by the tide-like large-scale structures and unexpected mean values in the vertical velocity estimates in the MLT from our SIMONe systems in Argentina, Germany, and Peru. It is not a comparative study between the winds obtained from models and multistatic SMRs. Instead, we created a tool called VMMR based on data from the UA-ICON high-resolution model to validate the quantities estimated from SIMONe systems in particular and multistatic SMRs in general. This tool, the VMMR, can validate all the analyses connected to multistatic SMRs. However, in our study, we focus only on the estimation techniques related to the mean winds and gradients in the MLT.

In our VMMR, we consider the UA-ICON model output as our pseudo atmosphere. Therefore, we used various SIMONe system geometries and realistic meteor samplings to simulate multistatic SMR observations on this pseudo atmosphere. These virtually simulated meteor observations were then used to estimate mean winds and gradients and were compared with the model data.

From our analyses, we can conclude that the methods to estimate the mean zonal and meridional components of velocity work effectively in the multistatic SMRs. The horizontal wind gradient estimation using multistatic SMRs show in general a good correlation, where some geometries are better than others. Hence, it is also clear that the accurate estimation of gradient terms requires larger meteor observation networks such as SIMONe 2018. The other existing systems, such as SIMONe Peru and Argentina, give a good correlation, but not as excellent as SIMONe 2018.

The validation tests on the vertical velocity estimation show a poor correlation. However, our VMMR results could only explain the variability of ± 1 –2 m/s in the estimates. These variabilities are due to the small-scale structures present in the horizontal winds and their leakage to the vertical velocity estimates. These tests did not explain the large-scale tide-like structures observed in the actual SIMONe observations in Peru, Argentina, and Germany. Further tests using virtual radar systems by inducing diurnal tides to the UA-ICON data suggest that the SIMONe systems can estimate the large-scale variations in the MLT vertical winds if they have an amplitude

CHARUVIL ASOKAN ET AL. 17 of 21



larger than 2 m/s. However, these tests are not imposing a geophysical significance to the actual observed tide-like features in the vertical velocities from SIMONe systems; rather, they display the capability of the systems.

Data Availability Statement

The data used to generate the figures presented in this manuscript can be found in HDF5 here: https://dx.doi.org/10.22000/499.

Acknowledgments

Projekt DEAL.

This work was partially supported by the Deutsche Forschungsgemeinschaft (DFG. German Research Foundation) under SPP 1788 (DynamicEarth)-CH1482/2-1 and under SPP 1788 (CoSIP)-CH1482/3-1. by the WATILA Project (SAW-2015-IAP-1) and MSGWaves/Processes And Climatology Of Gravity waves project LU 1174/8-1. H. Charuvil Asokan appreciates the support by the French Ministry of Foreign and European Affairs for the Eiffel excellence scholarship (File N 945179K), R. Marino acknowledges support from the project "EVENT-FUL" (ANR-20-CE30-0011), funded by the French "Agence Nationale de la Recherche" - ANR through the program AAPG-2020. The work of J. F. Conte is supported by the Bundesministerium für Bildung und Forschung via project WASCLIM-IAP part of the ROMIC-II program. S. Borchert thanks the DFG for partial support through the research unit MS-GWaves and Grant ZA 268/10-12. M. F. Larsen acknowledges partial support from National Science Foundation (NSF) grant AGS-2012994. Open access funding enabled and organized by

References

- Abdu, M. A., Batista, P. P., Batista, I. S., Brum, C. G. M., Carrasco, A. J., & Reinisch, B. W. (2006). Planetary wave oscillations in mesospheric winds, equatorial evening prereversal electric field and spread F. Geophysical Research Letters, 33(7), L07107. https://doi.org/10.1029/2005GL024837
- Alexander, M. J., Geller, M., McLandress, C., Polavarapu, S., Preusse, P., Sassi, F., et al. (2010). Recent developments in gravity-wave effects in climate models and the global distribution of gravity-wave momentum flux from observations and models. *Quarterly Journal of the Royal Meteorological Society*, 136(650), 1103–1124. https://doi.org/10.1002/qj.637
- Borchert, S., Zhou, G., Baldauf, M., Schmidt, H., Zängl, G., & Reinert, D. (2019). The upper-atmosphere extension of the ICON general circulation model (version: Ua-icon-1.0). *Geoscientific Model Development*, 12(8), 3541–3569. https://doi.org/10.5194/gmd-12-3541-2019
- Cervera, M. A., & Reid, I. M. (1995). Comparison of simultaneous wind measurements using colocated VHF meteor radar and MF spaced antenna radar systems. *Radio Science*, 30(4), 1245–1261. https://doi.org/10.1029/95RS00644
- Chang, J. L., Avery, S. K., & Vincent, R. A. (1999). New narrow-beam meteor radar results at Christmas Island: Implications for diurnal wind estimation. *Radio Science*, 34(1), 179–197. https://doi.org/10.1029/1998RS900012
- Charuvil Asokan, H., Chau, J. L., Vargas, F., Miguel Urco, J., Clahsen, M., & Christoph Jacobi, R. (2021). Frequency spectra of horizontal winds in the mesosphere and lower thermosphere region from multistatic specular meteor radar observations during the SIMONe 2018 campaign. https://doi.org/10.21203/RS.3.RS-697043/V1
- Chau, J. L., & Clahsen, M. (2019). Empirical phase calibration for multistatic specular meteor radars using a beamforming approach. *Radio Science*, 54(1), 60–71. https://doi.org/10.1029/2018RS006741
- Chau, J. L., Marino, R., Feraco, F., Urco, J. M., Baumgarten, G., Lübken, F.-J., et al. (2021). Radar observation of extreme vertical drafts in the polar summer mesosphere. *Geophysical Research Letters*, 48(16), e2021GL094918. https://doi.org/10.1029/2021GL094918
- Chau, J. L., Stober, G., Hall, C. M., Tsutsumi, M., Laskar, F. I., & Hoffmann, P. (2017). Polar mesospheric horizontal divergence and relative vorticity measurements using multiple specular meteor radars. *Radio Science*, 52(7), 811–828. https://doi.org/10.1002/2016RS006225
- Chau, J. L., Urco, J. M., Vierinen, J., Harding, B. J., Clahsen, M., Pfeffer, N., et al. (2021). Multistatic specular meteor radar network in Peru: System description and initial results. *Earth and Space Science*, 8(1), e2020EA001293. https://doi.org/10.1029/2020EA001293
- Chen, C., Chu, X., Zhao, J., Roberts, B. R., Yu, Z., Fong, W., et al. (2016). Lidar observations of persistent gravity waves with periods of 3–10 h in the Antarctic middle and upper atmosphere at McMurdo (77.83°S, 166.67°E). *Journal of Geophysical Research: Space Physics*, 121(2), 1483–1502. https://doi.org/10.1002/2015JA022127
- Clahsen, M. (2018). Error analysis of wind estimates in specular meteor radar systems. (MSc Thesis). https://doi.org/10.22000/45710.22000/457 Conte, J. F., Chau, J. L., Laskar, F. I., Stober, G., Schmidt, H., & Brown, P. (2018). Semidiurnal solar tide differences between fall and spring transition times in the Northern Hemisphere. Annales Geophysicae, 36(4), 999–1008. https://doi.org/10.5194/angeo-36-999-2018
- Conte, J. F., Chau, J. L., Stober, G., Pedatella, N., Maute, A., Hoffmann, P., et al. (2017). Climatology of semidiurnal lunar and solar tides at middle and high latitudes: Interhemispheric comparison. *Journal of Geophysical Research: Space Physics*, 122(7), 7750–7760. https://doi. org/10.1002/2017JA024396
- Conte, J. F., Chau, J. L., Urco, J. M., Latteck, R., Vierinen, J., & Salvador, J. O. (2021). First studies of mesosphere and lower thermosphere dynamics using a multistatic specular meteor radar network over southern patagonia. *Earth and Space Science*, 8(2), e2020EA001356. https:// doi.org/10.1029/2020EA001356
- Crueger, T., Giorgetta, M. A., Brokopf, R., Esch, M., Fiedler, S., Hohenegger, C., et al. (2018). ICON-A, the atmosphere component of the ICON earth system model: II. Model evaluation. *Journal of Advances in Modeling Earth Systems*, 10(7), 1638–1662. https://doi.org/10.1029/2017MS001233
- Davis, R. N., Du, J., Smith, A. K., Ward, W. E., & Mitchell, N. J. (2013). The diurnal and semidiurnal tides over Ascension Island (°S, 14°W) and their interaction with the stratospheric quasi-biennial oscillation: Studies with meteor radar, eCMAM and WACCM. Atmospheric Chemistry and Physics, 13(18), 9543–9564. https://doi.org/10.5194/acp-13-9543-2013
- De Wit, R. J., Hibbins, R. E., Espy, P. J., Orsolini, Y. J., Limpasuvan, V., & Kinnison, D. E. (2014). Observations of gravity wave forcing of the mesopause region during the January 2013 major Sudden Stratospheric Warming. *Geophysical Research Letters*, 41(13), 4745–4752. https://doi.org/10.1002/2014GL060501
- Dipankar, A., Stevens, B., Heinze, R., Moseley, C., Zängl, G., Giorgetta, M., & Brdar, S. (2015). Large eddy simulation using the general circulation model ICON. *Journal of Advances in Modeling Earth Systems*, 7(3), 963–986. https://doi.org/10.1002/2015MS000431
- Dowdy, A., Vincent, R. A., Igarashi, K., Murayama, Y., & Murphy, D. J. (2001). A comparison of mean winds and gravity wave activity in the northern and southern polar MLT. *Geophysical Research Letters*, 28(8), 1475–1478. https://doi.org/10.1029/2000GL012576
- Egito, F., Andrioli, V., & Batista, P. (2016). Vertical winds and momentum fluxes due to equatorial planetary scale waves using all-sky meteor radar over Brazilian region. *Journal of Atmospheric and Solar-Terrestrial Physics*, 149, 108–119. https://doi.org/10.1016/j.jastp.2016.10.005
- Eswaraiah, S., Kumar, K. N., Kim, Y. H., Chalapathi, G. V., Lee, W., Jiang, G., et al. (2020). Low-latitude mesospheric signatures observed during the 2017 sudden stratospheric warming using the fuke meteor radar and ERA-5. *Journal of Atmospheric and Solar-Terrestrial Physics*, 207, 105352. https://doi.org/10.1016/j.jastp.2020.105352
- Fauliot, V., Thuillier, G., & Vial, F. (1997). Mean vertical wind in the mesosphere-lower thermosphere region (80–120 km) deduced from the WINDII observations on board UARS. *Annales Geophysicae*, 15(9), 1221–1231. https://doi.org/10.1007/s00585-997-1221-9
- Feraco, F., Marino, R., Primavera, L., Pumir, A., Mininni, P. D., Rosenberg, D., & Marro, M. (2021). Connecting large-scale velocity and temperature bursts with small-scale intermittency in stratified turbulence. EPL (Europhysics Letters). https://doi.org/10.1209/0295-5075/135/14001

CHARUVIL ASOKAN ET AL. 18 of 21



- Feraco, F., Marino, R., Pumir, A., Primavera, L., Mininni, P. D., Pouquet, A., & Rosenberg, D. (2018). Vertical drafts and mixing in stratified turbulence: Sharp transition with Froude number. EPL (Europhysics Letters), 123(4), 44002. https://doi.org/10.1209/0295-5075/123/44002
- Forbes, J. M., Portnyagin, Y. I., Makarov, N. A., Palo, S. E., Merzlyakov, E. G., & Zhang, X. (1999). Dynamics of the lower thermosphere over South Pole from meteor radar wind measurements. Earth Planets and Space, 51(7–8), 611–620. https://doi.org/10.1186/BF03353219
- Franke, S. J. (2005). Comparison of meteor radar and Na Doppler lidar measurements of winds in the mesopause region above Maui, Hawaii. Journal of Geophysical Research, 110(D9), D09S02. https://doi.org/10.1029/2003JD004486
- Fritts, D. C., & Alexander, M. J. (2003). Gravity wave dynamics and effects in the middle atmosphere. Reviews of Geophysics, 41(1), 1003. https://doi.org/10.1029/2001RG000106
- Fritts, D. C., Hoppe, U.-P., & Inhester, B. (1990). A study of the vertical motion field near the high-latitude summer mesopause during MAC/ SINE. Journal of Atmospheric and Terrestrial Physics, 52(10–11), 927–938. https://doi.org/10.1016/0021-9169(90)90025-I
- Fritts, D. C., Vadas, S. L., & Yamada, Y. (2002). An estimate of strong local body forcing and gravity wave radiation based on OH airglow and meteor radar observations. *Geophysical Research Letters*, 29(10). https://doi.org/10.1029/2001GL013753
- Garcia, R. R. (1989). Dynamics, radiation, and photochemistry in the mesosphere: Implications for the formation of noctilucent clouds. *Journal of Geophysical Research: Atmospheres*, 94(D12), 14605–14615. https://doi.org/10.1029/JD094iD12p14605
- Gardner, C. S., & Liu, A. Z. (2007). Seasonal variations of the vertical fluxes of heat and horizontal momentum in the mesopause region at Star-fire Optical Range, New Mexico. *Journal of Geophysical Research*, 112(D9), D09113. https://doi.org/10.1029/2005JD006179
- Gerding, M., Baumgarten, G., Zecha, M., Lübken, F.-J., Baumgarten, K., & Latteck, R. (2021). On the unusually bright and frequent noctilucent clouds in summer 2019 above Northern Germany. *Journal of Atmospheric and Solar-Terrestrial Physics*, 217, 105577. https://doi.org/10.1016/j.jastp.2021.105577
- Giorgetta, M. A., Brokopf, R., Crueger, T., Esch, M., Fiedler, S., Helmert, J., et al. (2018). ICON-A, the atmosphere component of the ICON earth system model: I. Model description. *Journal of Advances in Modeling Earth Systems*, 10(7), 1613–1637. https://doi.org/10.1029/2017MS001242
- Gudadze, N., Stober, G., & Chau, J. L. (2019). Can VHF radars at polar latitudes measure mean vertical winds in the presence of PMSE? Atmospheric Chemistry and Physics, 19(7), 4485–4497. https://doi.org/10.5194/acp-19-4485-2019
- Haldoupis, C. (2011). A tutorial review on sporadic E layers. In Aeronomy of the earth's atmosphere and ionosphere (pp. 381–394). Springer Netherlands. https://doi.org/10.1007/978-94-007-0326-1 29
- He, M., & Chau, J. L. (2019). Mesospheric semidiurnal tides and near-12 h waves through jointly analyzing observations of five specular meteor radars from three longitudinal sectors at boreal midlatitudes. Atmospheric Chemistry and Physics, 19(9), 5993–6006. https://doi.org/10.5194/acp-19-5993-2019
- Hecht, J. H., Walterscheid, R. L., Gelinas, L. J., Vincent, R. A., Reid, I. M., & Woithe, J. M. (2010). Observations of the phase-locked 2 day wave over the Australian sector using medium-frequency radar and airglow data. *Journal of Geophysical Research*, 115(D16), D16115. https://doi.org/10.1029/2009JD013772
- Heinze, R., Dipankar, A., Henken, C. C., Moseley, C., Sourdeval, O., Trömel, S., et al. (2017). Large-eddy simulations over Germany using ICON: A comprehensive evaluation. *Quarterly Journal of the Royal Meteorological Society*, 143(702), 69–100. https://doi.org/10.1002/qj.2947
- Hibbins, R., Espy, P., Jarvis, M., Riggin, D., & Fritts, D. (2007). A climatology of tides and gravity wave variance in the MLT above Rothera, Antarctica obtained by MF radar. *Journal of Atmospheric and Solar-Terrestrial Physics*, 69(4–5), 578–588. https://doi.org/10.1016/j.iastp.2006.10.009
- Hocking, W., Fuller, B., & Vandepeer, B. (2001). Real-time determination of meteor-related parameters utilizing modern digital technology. Journal of Atmospheric and Solar-Terrestrial Physics, 63(2–3), 155–169. https://doi.org/10.1016/s1364-6826(00)00138-3
- Hocking, W. K. (2001). Middle atmosphere dynamical studies at Resolute Bay over a full representative year: Mean winds, tides, and special oscillations. *Radio Science*, 36(6), 1795–1822. https://doi.org/10.1029/2000RS001003
- Hocking, W. K., & Hocking, A. (2002). Temperature tides determined with meteor radar. Annales Geophysicae, 20(9), 1447–1467. https://doi.org/10.5194/angeo-20-1447-2002
- Hocking, W. K., Kelley, M., Rogers, R., Brown, W. O., Moorcroft, D., & St Maurice, J. P. (2001). Resolute bay VHF radar: A multipurpose tool for studies of tropospheric motions, middle atmosphere dynamics, meteor physics, and ionospheric physics. *Radio Science*, 36(6), 1839–1857. https://doi.org/10.1029/2000RS001005
- Hoffmann, P., Becker, E., Singer, W., & Placke, M. (2010). Seasonal variation of mesospheric waves at northern middle and high latitudes. *Journal of Atmospheric and Solar-Terrestrial Physics*, 72(14–15), 1068–1079. https://doi.org/10.1016/J.JASTP.2010.07.002
- Holdsworth, D. A., Reid, I. M., & Cervera, M. A. (2004). Buckland Park all-sky interferometric meteor radar. Radio Science, 39(5). https://doi.org/10.1029/2003rs003014
- Hoppe, U.-P., & Fritts, D. C. (1995a). High-resolution measurements of vertical velocity with the European incoherent scatter VHF radar: 1. Motion field characteristics and measurement biases. *Journal of Geophysical Research*, 100(D8), 16813. https://doi.org/10.1029/95JD01466
- Hoppe, U.-P., & Fritts, D. C. (1995b). On the downward bias in vertical velocity measurements by VHF radars. *Geophysical Research Letters*, 22(5), 619–622, https://doi.org/10.1029/95GL00165
- Huang, K. M., Liu, H., Liu, A. Z., Zhang, S. D., Huang, C. M., Gong, Y., & Ning, W. H. (2021). Investigation on spectral characteristics of gravity waves in the MLT using lidar observations at andes. *Journal of Geophysical Research: Space Physics*, 126(4), e2020JA028918. https://doi. org/10.1029/2020JA028918
- Hysell, D. L., Larsen, M. F., & Sulzer, M. P. (2014). High time and height resolution neutral wind profile measurements across the mesosphere/ lower thermosphere region using the Arecibo incoherent scatter radar. *Journal of Geophysical Research: Space Physics*, 119(3), 2345–2358. https://doi.org/10.1002/2013JA019621
- Jacobi, C., Arras, C., Kürschner, D., Singer, W., Hoffmann, P., & Keuer, D. (2009). Comparison of mesopause region meteor radar winds, medium frequency radar winds and low frequency drifts over Germany. *Advances in Space Research*, 43(2), 247–252. https://doi.org/10.1016/j.asr.2008.05.009
- Jaen, J., Renkwitz, T., Chau, J. L., He, M., Hoffmann, P., Yamazaki, Y., et al. (2021). Long-term studies of mesosphere and lower-thermosphere summer length definitions based on mean zonal wind features observed for more than one solar cycle at middle and high latitudes in the Northern Hemisphere. Annales Geophysicae, 40, 23–35. https://doi.org/10.5194/angeo-40-23-2022
- Jiang, G., Xu, J., Yuan, W., Ning, B., Wan, W., & Hu, L. (2012). A comparison of mesospheric winds measured by FPI and meteor radar located at 40N. Science China Technological Sciences, 55(5), 1245–1250. https://doi.org/10.1007/s11431-012-4773-1
- Kishore Kumar, G., & Hocking, W. K. (2010). Climatology of northern polar latitude MLT dynamics: Mean winds and tides. Annales Geophysicae, 28(10), 1859–1876. https://doi.org/10.5194/angeo-28-1859-2010
- Kishore Kumar, G., Nesse Tyssøy, H., & Williams, B. P. (2018). A preliminary comparison of Na lidar and meteor radar zonal winds during geomagnetic quiet and disturbed conditions. *Journal of Atmospheric and Solar-Terrestrial Physics*, 168, 70–79. https://doi.org/10.1016/j.jastp.2018.01.010

CHARUVIL ASOKAN ET AL. 19 of 21



- Larsen, M. F. (2004). Observations of overturning in the upper mesosphere and lower thermosphere. *Journal of Geophysical Research*, 109(D2), D02S04. https://doi.org/10.1029/2002JD003067
- Larsen, M. F., & Meriwether, J. W. (2012). Vertical winds in the thermosphere. Journal of Geophysical Research, 117(A9). https://doi.org/10.1029/2012ja017843
- Laskar, F. I., Chau, J. L., St-Maurice, J. P., Stober, G., Hall, C. M., Tsutsumi, M., et al. (2017). Experimental evidence of arctic summer mesospheric upwelling and its connection to cold summer mesopause. *Geophysical Research Letters*, 44(18), 9151–9158. https://doi. org/10.1002/2017GL074759
- Lee, Y.-S., Kim, Y. H., Kim, K.-C., Kwak, Y.-S., Sergienko, T., Kirkwood, S., & Johnsen, M. G. (2018). EISCAT observation of wave-like fluctuations in vertical velocity of polar mesospheric summer echoes associated with a geomagnetic disturbance. *Journal of Geophysical Research: Space Physics*, 123(6), 5182–5194. https://doi.org/10.1029/2018JA025399
- Lehmacher, G. A., Scott, T. D., Larsen, M. F., Bilén, S. G., Croskey, C. L., Mitchell, J. D., et al. (2011). The turbopause experiment: Atmospheric stability and turbulent structure spanning the turbopause altitude. *Annales Geophysicae*, 29(12), 2327–2339. https://doi.org/10.5194/angeo-29-2327-2011
- Lilienthal, F., & Jacobi, C. (2015). Meteor radar quasi 2-day wave observations over 10 years at Collm (51.3°N, 13.0°E). Atmospheric Chemistry and Physics, 15(17), 9917–9927. https://doi.org/10.5194/acp-15-9917-2015
- Lima, L., Batista, P., Takahashi, H., & Clemesha, B. (2004). Quasi-two-day wave observed by meteor radar at 22.7°S. Journal of Atmospheric and Solar-Terrestrial Physics, 66(6–9), 529–537. https://doi.org/10.1016/j.jastp.2004.01.007
- Liu, A. Z., Hocking, W. K., Franke, S. J., & Thayaparan, T. (2002). Comparison of Na lidar and meteor radar wind measurements at Starfire Optical Range, NM, USA. *Journal of Atmospheric and Solar-Terrestrial Physics*, 64(1), 31–40. https://doi.org/10.1016/S1364-6826(01)00095-5
- Liu, G., Janches, D., Lieberman, R. S., Moffat-Griffin, T., Fritts, D. C., & Mitchell, N. J. (2020). Coordinated observations of 8- and 6-hr tides in the mesosphere and lower thermosphere by three meteor radars near 60°S latitude. *Geophysical Research Letters*, 47(1), e2019GL086629. https://doi.org/10.1029/2019GL086629
- Lübken, F.-J., Höffner, J., Viehl, T. P., Kaifler, B., & Morris, R. J. (2011). First measurements of thermal tides in the summer mesopause region at Antarctic latitudes. *Geophysical Research Letters*, 38(24). https://doi.org/10.1029/2011GL050045
- Marino, R., Feraco, F., Primavera, L., Pumir, A., Pouquet, A., Rosenberg, D., & Mininni, P. D. (2021). Turbulence generation by large-scale extreme vertical drafts and the modulation of local energy dissipation in stably stratified geophysical flows.
- Marino, R., Mininni, P. D., Rosenberg, D., & Pouquet, A. (2013). Inverse cascades in rotating stratified turbulence: Fast growth of large scales. EPL (Europhysics Letters), 102(4), 44006. https://doi.org/10.1209/0295-5075/102/44006
- Marino, R., Mininni, P. D., Rosenberg, D. L., & Pouquet, A. (2014). Large-scale anisotropy in stably stratified rotating flows. *Physical Review E*, 90(2), 023018. https://doi.org/10.1103/PhysRevE.90.023018
- Marino, R., Pouquet, A., & Rosenberg, D. (2015). Resolving the paradox of oceanic large-scale balance and small-scale mixing. *Physical Review Letters*, 114(11), 114504. https://doi.org/10.1103/PhysRevLett.114.114504
- Marino, R., Rosenberg, D., Herbert, C., & Pouquet, A. (2015). Interplay of waves and eddies in rotating stratified turbulence and the link with kinetic-potential energy partition. EPL (Europhysics Letters), 112(4), 49001. https://doi.org/10.1209/0295-5075/112/49001
- Marsh, S., Bennett, R., Baggaley, W., Fraser, G., & Plank, G. (2000). Measuring meridional mesospheric winds with the AMOR meteor radar. Journal of Atmospheric and Solar-Terrestrial Physics, 62(13), 1129–1133. https://doi.org/10.1016/S1364-6826(00)00102-4
- Matzka, J., Bronkalla, O., Kervalishvili, G., Rauberg, J., & Stolle, C. (2021). Geomagnetic Hpo index. V. 1.0. GFZ Data Services. https://doi.org/10.5880/Hpo.0001
- Matzka, J., Stolle, C., Yamazaki, Y., Bronkalla, O., & Morschhauser, A. (2021). The geomagnetic Kp index and derived indices of geomagnetic activity. Space Weather, 19(5), e2020SW002641. https://doi.org/10.1029/2020SW002641
- McCormack, J., Hoppel, K., Kuhl, D., deWit, R., Stober, G., Espy, P., et al. (2017). Comparison of mesospheric winds from a high-altitude meteorological analysis system and meteor radar observations during the boreal winters of 2009–2010 and 2012–2013. *Journal of Atmospheric and Solar-Terrestrial Physics*, 154, 132–166. https://doi.org/10.1016/j.jastp.2016.12.007
- Mitchell, N. J., & Beldon, C. L. (2009). Gravity waves in the mesopause region observed by meteor radar: 1. A simple measurement technique. Journal of Atmospheric and Solar-Terrestrial Physics, 71(8–9), 866–874. https://doi.org/10.1016/j.jastp.2009.03.011
- Mitchell, N. J., & Howells, V. S. C. (1998). Vertical velocities associated with gravity waves measured in the mesosphere and lower thermosphere with the EISCAT VHF radar. *Annales Geophysicae*, 16(10), 1367–1379. https://doi.org/10.1007/s00585-998-1367-0
- Murphy, D. J., Aso, T., Fritts, D. C., Hibbins, R. E., McDonald, A. J., Riggin, D. M., et al. (2009). Source regions for Antarctic MLT non-migrating semidiurnal tides. *Geophysical Research Letters*, 36(9), L09805. https://doi.org/10.1029/2008GL037064
- Murphy, D. J., Forbes, J. M., Walterscheid, R. L., Hagan, M. E., Avery, S. K., Aso, T., et al. (2006). A climatology of tides in the Antarctic mesosphere and lower thermosphere. *Journal of Geophysical Research: Atmospheres*, 111(D23). https://doi.org/10.1029/2005JD006803
- Nakamura, T., Tsuda, T., Maekawa, R., Tsutsumi, M., Shiokawa, K., & Ogawa, T. (2001). Seasonal variation of gravity waves with various temporal and horizontal scales in the MLT region observed with radar and airglow imaging. *Advances in Space Research*, 27(10), 1737–1742. https://doi.org/10.1016/S0273-1177(01)00310-6
- Nakamura, T., Tsuda, T., Tsutsumi, M., Kita, K., Uehara, T., Kato, S., & Fukao, S. (1991). Meteor wind observations with the MU radar. *Radio Science*, 26(4), 857–869. https://doi.org/10.1029/91RS01164
- Pancheva, D. V. (2004). Planetary waves and variability of the semidiurnal tide in the mesosphere and lower thermosphere over Esrange (68°N, 21°E) during winter. *Journal of Geophysical Research*, 109(A8), A08307. https://doi.org/10.1029/2004JA010433
- Placke, M., Hoffmann, P., Becker, E., Jacobi, C., Singer, W., & Rapp, M. (2011). Gravity wave momentum fluxes in the MLT—Part II: Meteor radar investigations at high and midlatitudes in comparison with modeling studies. *Journal of Atmospheric and Solar-Terrestrial Physics*, 73(9), 911–920. https://doi.org/10.1016/j.jastp.2010.05.007
- Pouquet, A., Marino, R., Mininni, P. D., & Rosenberg, D. (2017). Dual constant-flux energy cascades to both large scales and small scales. *Physics of Fluids*, 29(11), 111108. https://doi.org/10.1063/1.5000730
- Sandford, D. J., Muller, H. G., & Mitchell, N. J. (2006). Observations of lunar tides in the mesosphere and lower thermosphere at Arctic and middle latitudes. Atmospheric Chemistry and Physics, 6(12), 4117–4127. https://doi.org/10.5194/acp-6-4117-2006
- Smith, A. K. (2012). Global dynamics of the MLT. Surveys in Geophysics, 33(6), 1177–1230. https://doi.org/10.1007/s10712-012-9196-9
- Spargo, A. J., Reid, I. M., & MacKinnon, A. D. (2019). Multistatic meteor radar observations of gravity-wave-tidal interaction over southern Australia. Atmospheric Measurement Techniques, 12(9), 4791–4812. https://doi.org/10.5194/amt-12-4791-2019
- Stober, G., & Chau, J. L. (2015). A multistatic and multifrequency novel approach for specular meteor radars to improve wind measurements in the MLT region. *Radio Science*, 50(5), 431–442. https://doi.org/10.1002/2014RS005591
- Stober, G., Chau, J. L., Vierinen, J., Jacobi, C., & Wilhelm, S. (2018). Retrieving horizontally resolved wind fields using multi-static meteor radar observations. *Atmospheric Measurement Techniques*, 11(8), 4891–4907. https://doi.org/10.5194/amt-11-4891-2018

CHARUVIL ASOKAN ET AL. 20 of 21



- Stober, G., Kozlovsky, A., Liu, A., Qiao, Z., Tsutsumi, M., Hall, C., & Mitchell, N. (2021). Atmospheric tomography using the Nordic meteor radar clusterand Chilean observation network de meteor radars: Networkdetails and 3DVAR retrieval. *Atmospheric Measurement Techniques*. https://doi.org/10.5194/amt-2021-124
- Suresh Babu, V., Ramkumar, G., & Rachel John, S. (2012). Seasonal variation of planetary wave momentum flux and the forcing towards mean flow acceleration in the MLT region. *Journal of Atmospheric and Solar-Terrestrial Physics*, 78–79, 53–61. https://doi.org/10.1016/j. iastp.2011.05.010
- Urco, J. M., Chau, J. L., Milla, M. A., Vierinen, J. P., & Weber, T. (2018). Coherent MIMO to improve aperture synthesis radar imaging of field-aligned irregularities: First results at jicamarca. *IEEE Transactions on Geoscience and Remote Sensing*, 56(5), 2980–2990. https://doi. org/10.1109/TGRS.2017.2788425
- Urco, J. M., Chau, J. L., Weber, T., & Latteck, R. (2019). Enhancing the spatiotemporal features of polar mesosphere summer echoes using coherent MIMO and radar imaging at MAARSY. Atmospheric Measurement Techniques, 12(2), 955–969. https://doi.org/10.5194/amt-12-955-2019
- Vargas, F., Chau, J. L., Charuvil Asokan, H., & Gerding, M. (2021). Mesospheric gravity wave activity estimated via airglow imagery, multistatic meteor radar, and SABER data taken during the SIMONe–2018 campaign. Atmospheric Chemistry and Physics, 21(17), 13631–13654. https://doi.org/10.5194/ACP-21-13631-2021
- Vierinen, J., Chau, J. L., Charuvil Asokan, H., Urco, J. M., Clahsen, M., Avsarkisov, V., et al. (2019). Observing mesospheric turbulence with specular meteor radars: A novel method for estimating second-order statistics of wind velocity. *Earth and Space Science*, 6(7), 1171–1195. https://doi.org/10.1029/2019EA000570
- Vierinen, J., Chau, J. L., Pfeffer, N., Clahsen, M., & Stober, G. (2016). Coded continuous wave meteor radar. Atmospheric Measurement Techniques, 9(2), 829–839. https://doi.org/10.5194/amt-9-829-2016
- Vierinen, J., Kero, A., & Rietveld, M. T. (2013). High latitude artificial periodic irregularity observations with the upgraded EISCAT heating facility. *Journal of Atmospheric and Solar-Terrestrial Physics*, 105–106, 253–261. https://doi.org/10.1016/j.jastp.2013.08.012
- Vincent, R. A. (2015). The dynamics of the mesosphere and lower thermosphere: A brief review. *Progress in Earth and Planetary Science*, 2(1). https://doi.org/10.1186/s40645-015-0035-8
- Vincent, R. A., Kovalam, S., Murphy, D. J., Reid, I. M., & Younger, J. P. (2019). Trends and variability in vertical winds in the southern hemisphere summer polar mesosphere and lower thermosphere. *Journal of Geophysical Research: Atmospheres*, 124(21), 11070–11085. https://doi.org/10.1029/2019JD030735
- Vincent, R. A., Kovalam, S., Reid, I. M., & Younger, J. P. (2010). Gravity wave flux retrievals using meteor radars. *Geophysical Research Letters*, 37(14). https://doi.org/10.1029/2010gl044086
- Volz, R., Chau, J., Erickson, P., Vierinen, J., Urco, J. M., & Clahsen, M. (2021). Four-dimensional mesospheric and lower thermospheric wind elds using Gaussian process regression on multistatic specular meteor radar observations. Atmospheric Measurement Techniques Discussions, 1–29. https://doi.org/10.5194/amt-2021-40
- Wilhelm, S., Stober, G., & Brown, P. (2019). Climatologies and long-term changes in mesospheric wind and wave measurements based on radar observations at high and mid latitudes. *Annales Geophysicae*, 37(5), 851–875. https://doi.org/10.5194/ANGEO-37-851-2019
- Wilhelm, S., Stober, G., & Chau, J. L. (2017). A comparison of 11-year mesospheric and lower thermospheric winds determined by meteor and MF radar at 69° N. *Annales Geophysicae*, 35(4), 893–906. https://doi.org/10.5194/angeo-35-893-2017
- Xiong, J.-G., Wan, W., Ning, B., & Liu, L. (2004). First results of the tidal structure in the MLT revealed by Wuhan Meteor Radar (30°40 N, 114°30 E). *Journal of Atmospheric and Solar-Terrestrial Physics*, 66(6–9), 675–682. https://doi.org/10.1016/j.jastp.2004.01.018
- Younger, J. P., Reid, I. M., Vincent, R. A., & Murphy, D. J. (2015). A method for estimating the height of a mesospheric density level using meteor radar. Geophysical Research Letters, 42(14), 6106–6111. https://doi.org/10.1002/2015GL065066
- Yu, T., Xia, C., Zuo, X., Huang, C., Mao, T., Liu, L., & Liu, Z. (2016). A comparison of mesospheric and low-thermospheric winds measured by Fabry-Perot interferometer and meteor radar over central China. *Journal of Geophysical Research: Space Physics*, 121(10), 10037–10051. https://doi.org/10.1002/2016JA022997
- Zängl, G., Reinert, D., Rípodas, P., & Baldauf, M. (2015). The ICON (ICOsahedral Non-hydrostatic) modelling framework of DWD and MPI-M: Description of the non-hydrostatic dynamical core. *Quarterly Journal of the Royal Meteorological Society*, 141(687), 563–579. https://doi.org/10.1002/qj.2378
- Zeng, X., Atlas, R., Birk, R. J., Carr, F. H., Carrier, M. J., Cucurull, L., & Zhang, F. (2020). Use of observing system simulation experiments in the United States. *Bulletin of the American Meteorological Society*, 9101(8), E1427–E1438. https://doi.org/10.1175/bams-d-19-0155.1
- Zhou, Q. H. (2000). Incoherent scatter radar measurement of vertical winds in the mesosphere. *Geophysical Research Letters*, 627(12), 1803–1806. https://doi.org/10.1029/2000GL003747

CHARUVIL ASOKAN ET AL. 21 of 21